Chapter 1 Introduction and Literature Review

1.1. Introduction

In this chapter, we present a brief introduction to the various phenomena relevant to the subject of study and a brief review on the multiferroic $BiFeO_3$ and its solid solutions with perovskites as well as magnetic transition in complex perovskites of the type $A(B'_{1/2}B''_{1/2})O_3$.

1.2. Perovskites:

The oxide materials with chemical formula ABO_3, where 'A' and 'B' are two cations and 'O' is an anion are classified as perovskites, e.g. $SrTiO_3$, $BaTiO_3$, $CaTiO_3$ etc. The geometrical requirement for the formation of the perovskite structure is given by the so-called Goldschmidt criterion [1] in terms of the ionic radii R_A, R_B and R_O of A, B and the O ions, respectively:

$$t = \frac{R_A + R_O}{\sqrt{2}(R_B + R_O)} \qquad \ldots\ldots \quad (1.1)$$

where t is known as the tolerance factor. It measures the degree of distortion in the perovskite structure. The perovskite structure is stable if t lies in the range $0.80 < t < 1.1$. For $t = 1$, the structure is expected to adopt ideal cubic perovskite structure (e.g. $SrTiO_3$). For $t > 1$, the compounds are known to show ferroelectricity (e.g. $BaTiO_3$). The compounds with $0.8 < t < 0.95$ show distorted perovskite structure (e.g. $CaTiO_3$, $SrZrO_3$).

The ideal cubic perovskite structure belongs to the $Pm\bar{3}m$ space group symmetry and the unit cell consists of one formula unit of ABO_3 in which all the ions occupy the special Wyckoff positions given below,

A cation at 1(a) Wyckoff site with position (0, 0, 0)

B cation at 1(b) Wyckoff site with (1/2, 1/2, 1/2) positions

O anion at 3(c) Wyckoff site with (1/2, 1/2, 0) positions.

A schematic representation of the cubic perovskite structure is given in Fig. 1.1. In this perovskite structure, the B-site cations occupy the center of the unit cell and form BO_6 octahedra while the A-site cations occupy the eight corners in the unit cell and are coordinated with twelve oxygen anions.

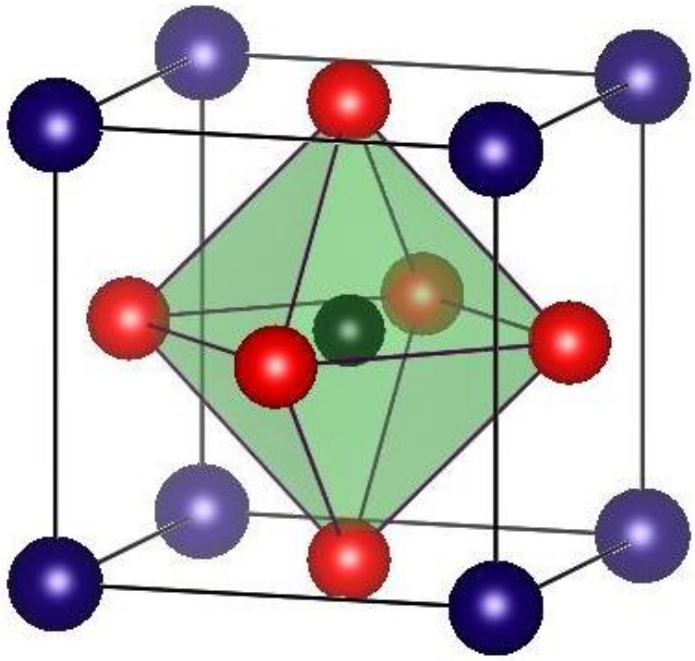

Figure 1.1: Schematic view of the ideal cubic perovskite structure: A cation occupy on the cubic corner position (0, 0, 0) (shown by blue sphere), B cation sits on the (1/2, 1/2, 1/2) position (shown by dark green sphere) and O anion sits on the face diagonal (1/2, 1/2, 0) positions (shown by red sphere).

1.3. Ferroelectricity:

The ferroelectric materials possess spontaneous electric polarization (P), even in the absence of an external electric field (E), whose direction can be switched by applying an electric field. This phenomenon is known as ferroelectricity and is usually observed in the polar class of non-centrosymetric crystals. The typical P-E hysteresis loop for ferroelectric materials is shown in Fig. 1.2. The development of the polar axis in ferroelectrics is usually attributed to a structural phase transition between high

temperature paraelectric phase to low temperature ferroelectric phase at a characteristic temperature called Curie temperature. The transition from the paraelectric to ferroelectric phase is accompanied by pronounced anomaly in the dielectric permittivity. The temperature dependence of dielectric permittivity above the transition temperature obeys Curie-Weiss law,

$$\varepsilon' \approx \frac{C}{T-T_c} \quad , T>T_C \qquad \ldots\ldots(1.2)$$

where ε' is dielectric permittivity or dielectric constant, C is the Curie constant and T_C is the Curie-Weiss temperature. The Curie-Weiss temperature for ferroelectric materials is generally positive. The examples of ferroelectric materials are $BaTiO_3$, $PbTiO_3$ and $KNbO_3$ [2].

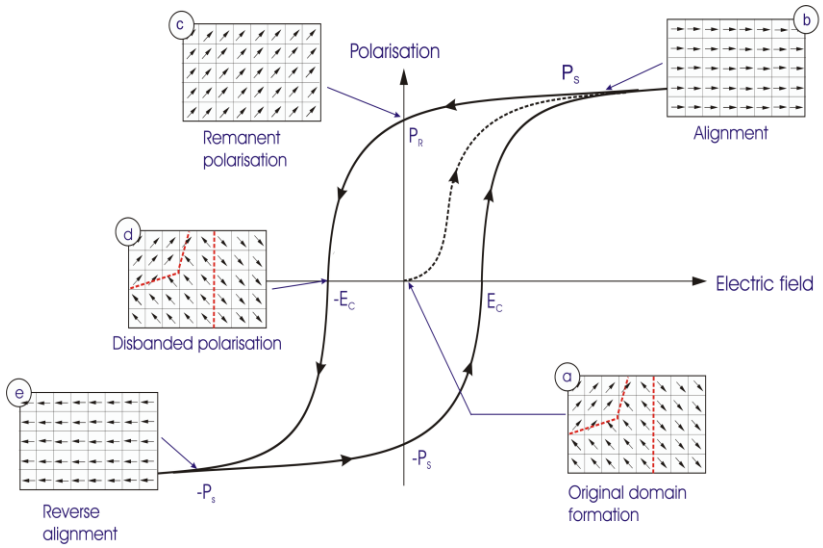

Figure 1.2: Typical P-E hysteresis loop for ferroelectric materials. P_S = Saturation polarization, P_R = Remnant polarization, E_C = Coercive field [3].

1.4. Antiferroelectricity:

Antiferroelectric materials possess antiparallel displacement of ions with respect to their ideal cubic positions. In a ferroelectric phase transition, the paraelectric unit cell size is slightly distorted due to the cationic and/or anionic displacements. But in the case of

antiferroelectric phase transition, the ionic displacements occur in equal and opposite directions in pairs. Thus the unit cell of the antiferroelectric phase becomes multiple of the unit cell of the paraelectric phase giving rise to appearance of characteristic superlattice reflections in diffraction pattern. Just like ferroelectric materials, the antiferroelectric materials also show a dielectric anomaly at the paraelectric to antiferroelectric phase transition. The temperature dependence of the dielectric constant in the paraelectric phase also follows Curie-Weiss law with negative Curie-Weiss temperature (θ) [4]:

$$\varepsilon' = \frac{C}{(T+\theta)} \qquad \ldots\ldots\ldots(1.3)$$

The transition temperature for antiferroelectric materials is commonly known as Néel temperature (T_N). In an antiferroelectric material, it is possible to induce ferroelectric ordering by application of sufficiently strong electric field. This feature is manifested in the 'double' hysteresis loop shown in Fig. 1.3. However, such a switching can be observed only if the antiferroelectric to ferroelectric switching field does not exceed the breakdown strength of the material. The most common examples of antiferroelectric materials are $PbZrO_3$, $NaNbO_3$, $PbHfO_3$ [2,5,6].

1.5. Ferrielectricity:

If a material exhibits ferroelectric order along one axis and antiferroelectric order along the other axes have been termed as ferrielectric materials [7–9]. The internal distribution of ions in ferrielectric material is such that the ferroelectric and antiferroelectric orders exist simultaneously in different directions. The unit cell of ferrielectric phase is a multiple of the unit cell of the paraelectric phase. The Curie-Weiss temperature may be negative/positive for ferrielectric phase transition in close analogy with antiferromagnetic/ferromagnetic phase transitions.

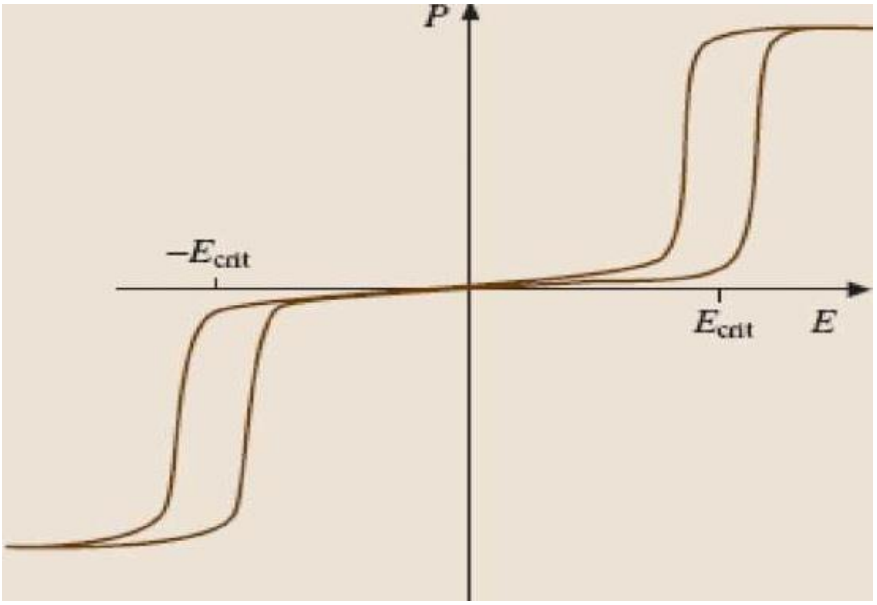

Figure 1.3: Typical hysteresis loop for antiferroelectric materials [10].

1.6. Phase transition driven by soft modes in perovskites:

In ferroelectric and antiferroelectric phase transitions, the atoms move from a high symmetry site in the high temperature phase to a low symmetry site in the low temperature phase through a small displacement. Such types of transitions are called displacive transitions. The displacive structural phase transition in perovskites can be described by soft phonon modes of the high temperature phase. This soft phonon mode is characterized by anomalous decrease in its frequency as the structural phase transition is approached. The temperature dependence of the soft phonon frequency can be expressed as

$$\omega^2 \alpha (T-T_C) \qquad \ldots\ldots\ldots(1.4)$$

A relation between the lattice dynamics and ferroelectric properties can be visualized through Lyddane-Sachs-Teller (LST) relationship [4] which relates the static dielectric constant ($\varepsilon'(0)$) and high frequency dielectric constant (($\varepsilon'(\infty)$) to the frequencies (ω) of the longitudinal optical (LO) and transverse optical (TO) phonon modes at the zone

centre (q = 0) of the Brillouin zone as:

$$\varepsilon'(0)/\varepsilon'(\infty) = (\omega_{LO}/\omega_{TO})^2 \qquad \ldots\ldots\ldots(1.5)$$

As the transverse optic mode frequency $\omega_{TO} \rightarrow 0$, the static dielectric constant shows a peak value. In fact, substituting Eq. (1.4) to Eq. (1.5) gives the well-known Curie-Weiss law for ferroelectric transition.

The structural phase transitions in perovskites are associated with soft modes corresponding to at least one of the symmetry points of the primitive cubic Brillouin zone. A schematic diagram of Brillouin zone of the ideal cubic perovskite structure is shown in Fig. 1.4 [11]. The high symmetry points of the Brillouin zone are described by the 10 symbols: Γ, Δ, Λ, Σ, R, T, M, S, X and Z. In the cubic perovskite structure containing 5 atoms, one expects 15 normal modes of vibration (12 optic and 3 acoustic). Each normal mode is characterized by an irreducible representation (Irrep). The irreps corresponding to the high symmetry points give different displacement pattern and hence play a key role in deciding the distortion of the ideal perovskite structure as a result of phase transition. The cubic to tetragonal phase transition in $BaTiO_3$ results from the freezing of the Γ_{15} soft phonon mode at q = (0, 0, 0) of the cubic Brillouin zone [12]. In $SrTiO_3$, the freezing of R_{25} mode with q = (½, ½, ½) leads to cubic to tetragonal phase transition at 105K involving anti-phase tilting of oxygen octahedra [5,13]. The freezing of the M_3 mode with q = (½, ½, 0) in $NaNbO_3$ leads to cubic to tetragonal phase transition [14].

1.7. Ferrodistortive and antiferrodistortive structural phase transitions:

The ferroelectric or antiferroelectric phase transitions in perovskites are special class of structural phase transition where the transition from the high symmetry phase to low symmetry phase is accompanied by the appearance of the spontaneous polarization or

sublattice polarization. The appearance of the long-rang polar or antipolar order is the characteristic feature of the ferroelectric or antiferroelectric transition. Based on the change in the number of formula units per unit cell, the structural phase transition may be

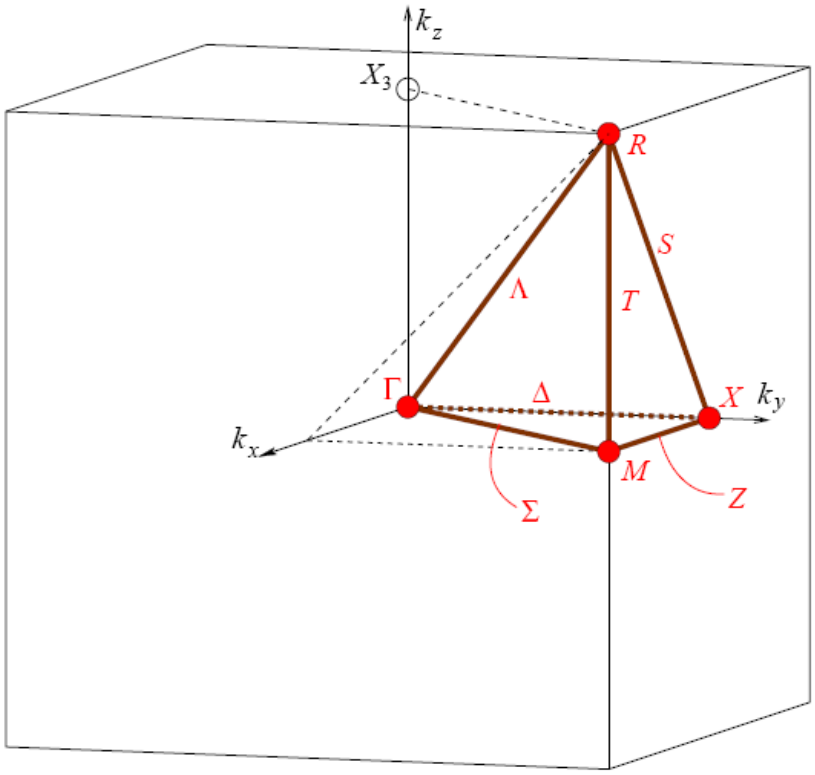

Figure 1.4: Schematic Brilloiun zone of the cubic perovskite structure showing special points [11].

classified as two categories [4]:

(1) Ferrodistortive transitions: In this type of phase transition the number of formula units per unit cell is same as that of the high temperature phase. Such type of phase transitions is always connected with the freezing of soft modes at the Brillouin zone centre (q =0). The typical examples are $BaTiO_3$, $PbTiO_3$ [15,16].

(2) Antiferrodistortive transitions: Here the number of formula units per unit cell is an

integer multiple of the high temperature phase. This type of phase transition corresponds to a freezing of the soft mode with non-zero wave vector ($q \neq 0$). The typical examples are $SrTiO_3$, $CaTiO_3$ [2,13] and also the antiferroelectric transitions [2,5,6].

1.8. Relaxor ferroelctrics:

Relaxor ferroelectrics are known to show very large value of dielectric constant (ε) with diffuse transition in the dielectric constant (ε) versus temperature (T) plot. Relaxors also shows frequency-dispersion in the ε-T plot. The peak temperatures T_m' and T_m'' corresponding to the real (ε') and imaginary (ε'') parts of the dielectric constant are not coincident but $T_m'' < T_m'$ in relaxors. Both the temperatures T_m'', T_m' shift to higher temperatures side with increasing frequency. The Lead (Pb) based perovskites with chemical formula $Pb(B'B'')O_3$ where B' = Mg^{2+}, Ni^{2+}, Zn^{2+}, Sc^{3+} and B'' = Nb^{5+}, Ta^{5+} etc., [17–19] are known to show relaxor ferroelectric behaviour. Several theoretical models such as superparaelectric [19], dipole glass [20], random field [21] random field-random bond [22] have been proposed to explain the relaxor ferroelectric behaviour. Depending upon the relaxational freezing of the polar clusters, most relaxors like $Pb(Mg_{1/3}Nb_{2/3})O_3$ (PMN) [20], $Pb(Sc_{1/2}Ta_{1/2})O_3$ (PST) [23] follow the Vogel-Fulcher law [24] for the polar dynamics:

$$\tau = \tau_0 \exp[E_a/k_B(T-T_{VF})] \qquad \text{…….(1.6)}$$

This is to be contrasted from systems which follow Arrhenius type behaviour [24].

$$\tau = \tau_0 \exp[E_a/k_BT] \qquad \text{…….(1.7)}$$

where E_a is the activation energy, τ_0 is the attempt time (inverse of the attempt frequency), k_B is the Boltzmann constant and T_{VF} is the Vogel-Fulcher freezing

temperature. The well-known examples of Arrhenius type systems are $(CoO)_{0.4}(Al_2O_3)_{0.1}(SiO_2)_{0.5}$ and $(KBr)_{0.5}(KCN)_{0.5}$ [24].

The comparisons of the normal ferroelectric with relaxors are illustrated in Fig. 1.5. Apart from the diffuse nature of the transition in the temperature dependence of the dielectric constant and the characteristics frequency dispersion of T_m' and T_m'', relaxor ferroelectrics exhibit slim P-E hysteresis loop which persist well above T_m' unlike normal ferroelectrics for which it disappears above T_C.

1.9. Ferromagnetism:

Materials which exhibit spontaneous magnetization that is stable and can be switched hysteretically by an applied magnetic field are called ferromagnetic materials. Ferromagnetism is defined as long range ordering of parallel alignment of magnetic spins (moments) resulting in net spontaneous magnetization even in the absence of magnetic field. A ferromagnetic material has domains and due to the presence of domains, magnetization is oriented in different directions. The subsequent alignment and reorientation of the domains depend on the application of a magnetic field, results in a hysteresis loop as shown in Fig. 1.6. Ferromagnetism disappears above a critical temperature T_C called Curie temperature. The magnetic susceptibility above T_C follows Curie-Weiss law as shown in Fig. 1.7 [26]:

$$\chi = \frac{C}{T - T_c} \qquad \ldots\ldots (1.8)$$

where C is the Curie constant and T_C the Curie-Weiss temperature.

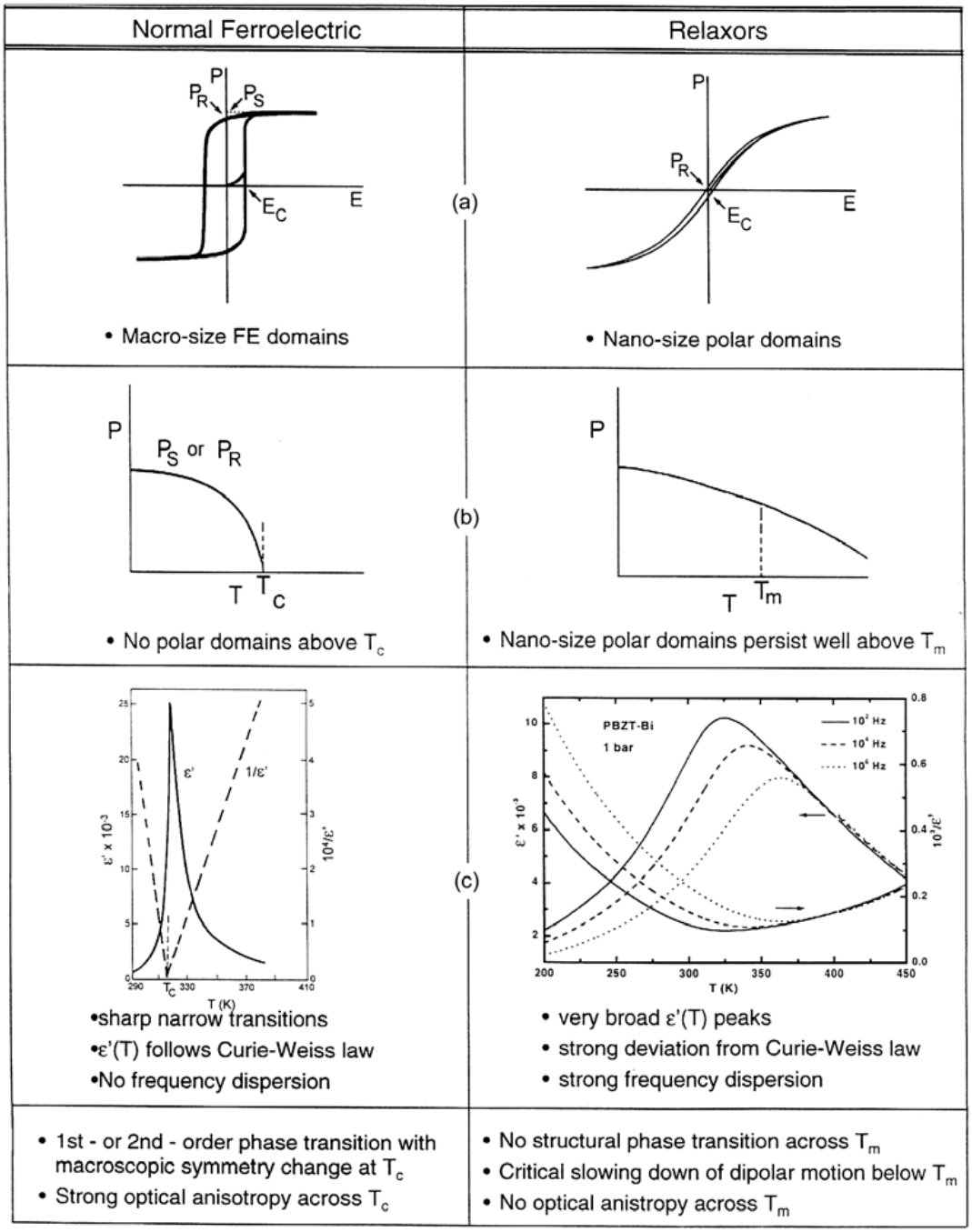

Figure 1.5: Comparison between the properties of normal and relaxors ferroelectrics behaviour [25].

The typical examples are Fe, Co, Ni, Gd, and Dy which show ferromagnetic properties but there are large number of alloys and compounds which also show ferromagnetic properties [26].

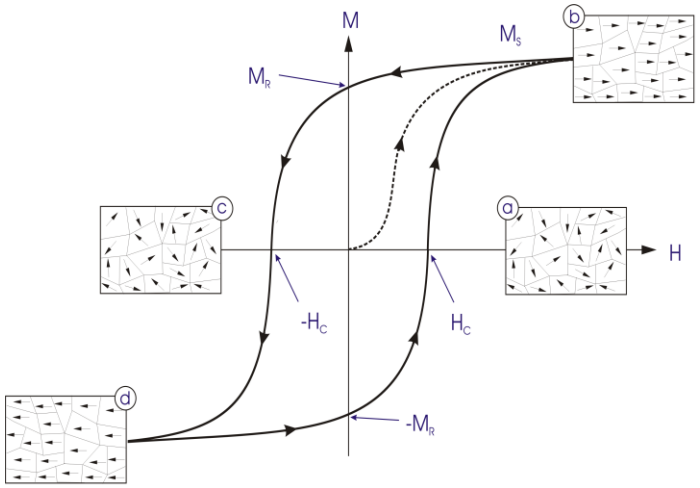

Figure 1.6: M-H Hysteresis Loop for Ferromagnetic materials. M_S is saturation magnetization, M_R is remanent magnetization at H = 0, H_C is coercivity at M = 0 [27].

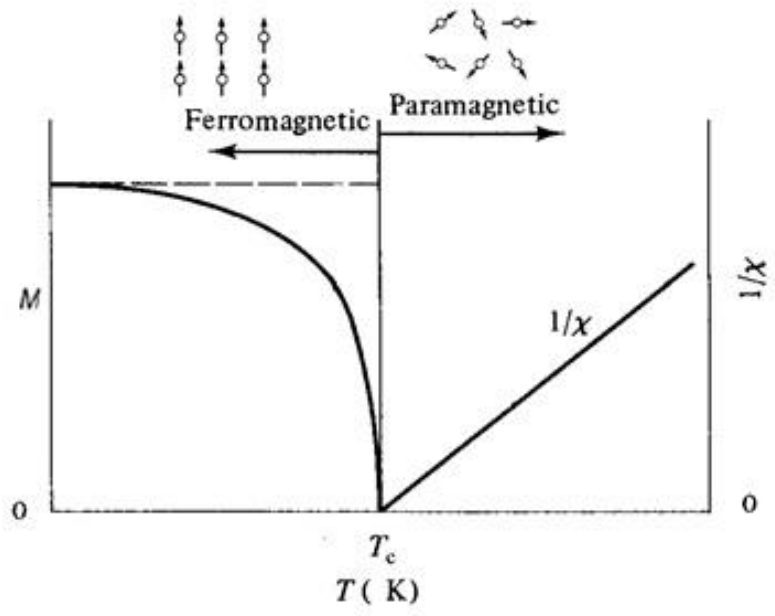

Figure 1.7: Temperature dependence of magnetization (M) and the inverse of the magnetic susceptibility ($1/\chi$) for ferromagnetic material. Reproduced from [26].

1.10. Antiferromagnetism:

In antiferromagnetic materials, the alignment of the spin moments of the neighbouring atoms is antiparallel to each other, and there is no net magnetic moment. The spin structure for the antiferromagnetic materials consists of two or more sublattices

each one of which are ferromagnetically coupled but are antiparallel to the neighbouring sublattice. Antiferromagnetic ordering exists below a critical temperature and above which materials get converted into paramagnetic material. This temperature is called as the Néel temperature (T_N). Antiferromagnetic materials also obey Curie-Weiss law but with a negative value of Curie temperature T_C and are given by the equation [26],

$$\chi = \frac{C}{T + T_c} \qquad \text{..... (1.9)}$$

where C is a Curie constant and T_C the Curie-Weiss temperature. A plot of inverse of susceptibility ($1/\chi$) versus T shown in Fig. 1.8 is a straight line above T_N and this line extrapolates to a negative temperature ($-T_C$) at $1/\chi = 0$. Although, there is no net magnetization in the antiferromagnetic materials but it may exhibit weak magnetization due to spin canting, lattice defects, and uncompensated spins at the surface in the absence of magnetic field. At sufficiently high magnetic fields, the spin direction of one of the magnetic sublattices may rotate and eventually lead to the "spin flop" where all the spins would be aligned in parallel fashion. Because of this rotation and spin flop, magnetization

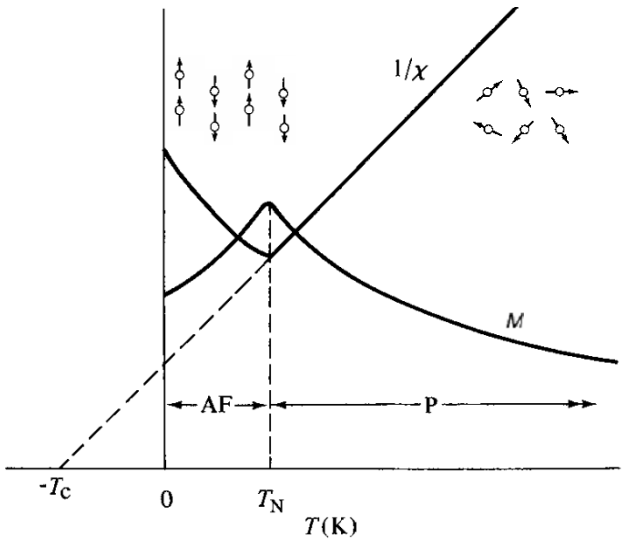

Figure 1.8: Temperature dependence of (M) and inverse of susceptibility ($1/\chi$) for antiferromagnetic material. AF: Antiferromagnetic, P : Paramagnetic [26].

can be induced by an external magnetic field. Depending on the interplane and intraplane coupling within the structure there are many types of antiferromagnetic spin orderings such as A-type, C- type and G-type or E-type shown in Fig. 1.9 [28]. The term “weak ferromagnetism” is used to explain the antiferromagnets with a small canting of spins away from antiparallel alignment. This spin canting is caused by the spin-orbit interaction.

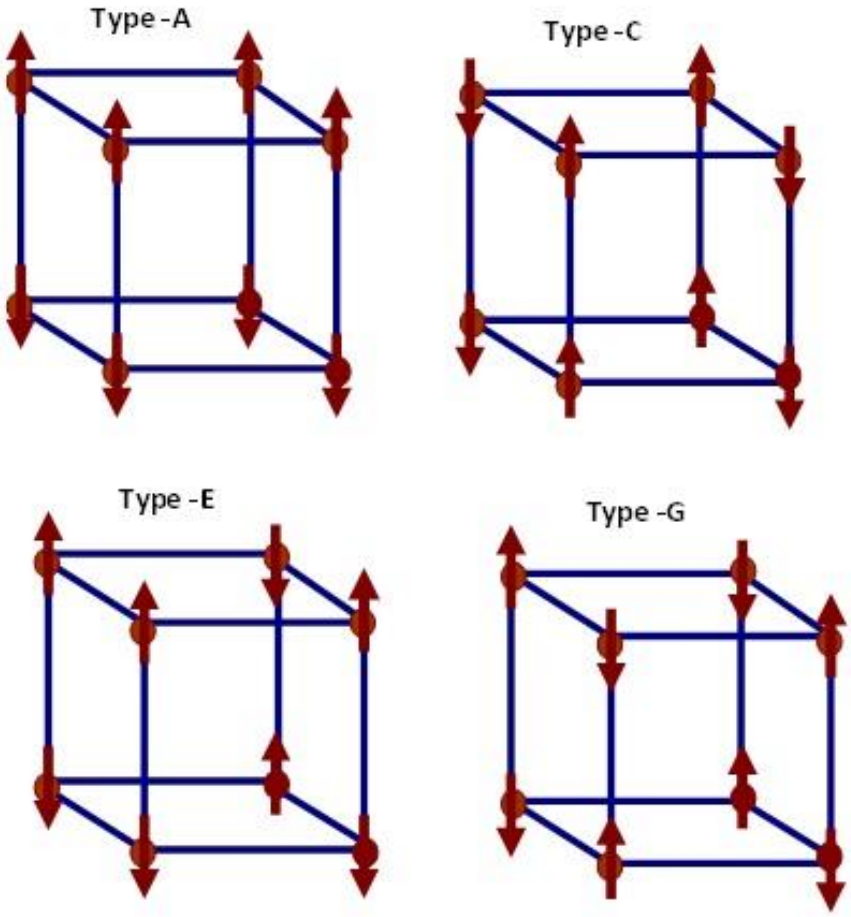

Figure 1.9: Different types of spin structure resulting in different type (A-, C-, G- or E-type) antiferromagnetic ordering [28].

1.11. Ferrimagnetism:

Ferrimagnetic materials differ from antiferromagnetics due to incomplete cancellation of the magnetic moment i.e., the adjacent spins are aligned antiparallel to each other but are unequal in magnitude. Ferrimagnetic materials exhibit spontaneous magnetization, like ferromagnetic materials. They exhibit the phenomena of magnetic saturation and also hysteresis loop. The spontaneous magnetization of a ferrimagnetic material disappears above a critical temperature T_c, with paramagnetic state (Fig. 1.10). The typical examples of ferrimagnetic materials are ferrites (Fe_3O_4), garnets ($Y_3Fe_5O_{12}$) and hexaferrites ($BaFe_{12}O_{19}$) [26]. Ferrimagnetic theory was developed by Néel, in

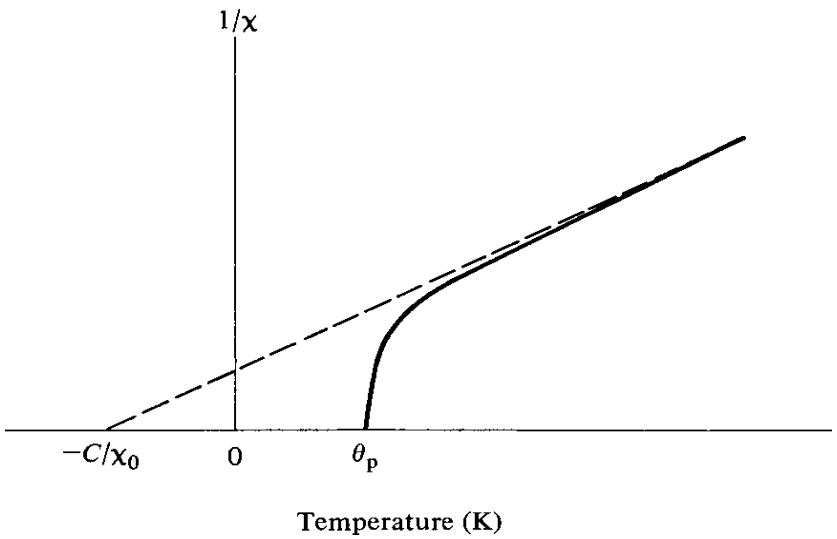

Figure 1.10: Theoretical variation of reciprocal of susceptibility with temperature for a ferrimagnetic above the Curie point [26].

continuation with the theory of antiferromagnetism. The Curie-Weiss law for ferrimagnetic materials up to T_c is given by the equation [26],

$$\chi = \frac{C}{T+\left(\frac{C}{\chi_0}\right)} \qquad \ldots.(1.10)$$

where C is Curie constant. For ferrimagnetic materials, the $(1/\chi)$ vs T plot becomes asymptotic at high temperature.

1.12. Multiferroics:

The "multiferroics" were originally defined as class of materials in which at least 2 of the 4 properties such as ferroelectricity, ferroelasticty, ferromagnetism, and ferrotoroidicity coexist in the same materials and are coupled also [29–32]. This definition has subsequently been expanded to include any for electric dipolar and magnetic spin ordering. Ferroelastics, like ferroelectrics and ferromagnets, have spontaneous strain in the absence stress that is switchable below a characteristic temperature [27–30]. Among the multiferroics, there exists a class of magnetoelectric materials where coupling between ferroelectric and magnetic order parameters occurs such that the magnetization (M) can be switched by the application of an electric field (E) and ferroelectric polarization (P) by the application of a magnetic field (H) [29,30,33]. The magnetoelectric multiferroic materials are interesting from the technological application point of view as they provide an additional degree of freedom in the designing of multifunctional sensors, actuators, storage devices, spintronics etc [30,33–36]. It also offers a challenge to theoretical physicists for understanding the physics behind the coexistence and coupling of the magnetic and ferroelectric order parameters. It has been generally believed that the ferroelectricity in ABO_3 perovskites arises due to the off-centring of the B-site cation and requires empty d-orbital (d^0) while the magnetism requires partially filled d orbitals (d^n) [37,38]. The two conditions appear to be mutually exclusive and therefore the magnetoelectric multiferroics are not so common. However, in the last two decades discovery of new multiferroic compounds like $RMnO_3$ (R=Tb, Dy, Y), $CoCrO_4$, $Ni_3V_2O_8$, $MnWO_4$, $LiCu_2O_2$, $LiCuVO_4$, CuO, $Ba_{0.5}Sr_{1.5}Zn_2Fe_{12}O_{22}$, $Ba_2Mg_2Fe_{12}O_{22}$ etc [36,39,40] in which ferroelectric polarization is induced as a result of

magnetic ordering through inverse D-M interaction. In such multiferroics, the mutually exclusiveness due to d^0 and d^n is avoided. Fig. 1.11 illustrate the various types of mechanism responsible for multiferroicity in multiferroic materials. In general, magnetoelectric multiferroics can be classified into two broad categories type- I and type-II. The difference between the two types of multiferroics is given in Table 1.1.

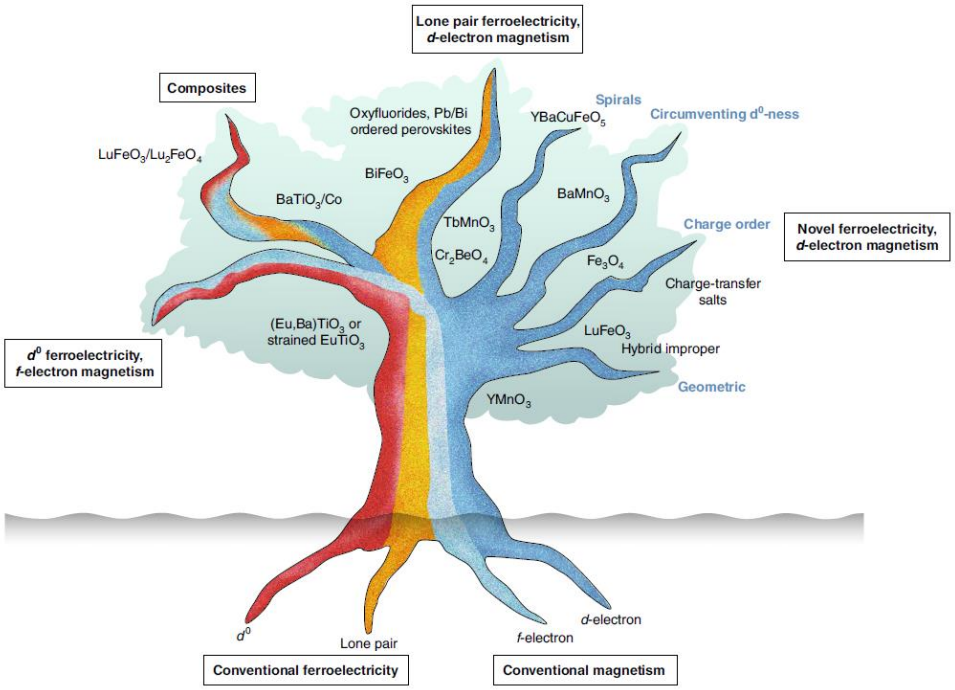

Figure 1.11: Different types of mechanism responsible for multiferroicity in a multiferroic materials [32].

1.13. Magnetoelectric coupling in multiferroics:

Magnetoelectric (ME) coupling describes the influence of a magnetic (electric) field on polarization (magnetization) of a material. ME coupling can be understood within the Landau theory framework, and can be obtained by expressing the free energy in terms of the electric field E and magnetic field H [29,33],

$$F(E,H) = F_0 - P_i^s E_i - M_i^s H_i - \frac{1}{2}\epsilon_0\epsilon_{ij} E_i E_j - \frac{1}{2}\mu_0\mu_{ij} H_i H_j - \alpha_{ij} E_i H_j$$

$$- \frac{\beta_{ijk}}{2} E_i H_j H_k - \frac{\gamma_{ijk}}{2} H_i E_j E_k + \quad \ldots\ldots\ldots(1.11)$$

where F_0 is the ground state free energy, subscript (i, j, k) represent the components of electric (E) and magnetic (H) fields, P_i^s and M_i^s are the component of spontaneous polarization and spontaneous magnetization, ϵ_0 and ϵ_{ij} are the permittivity of free space and relative permittivity (a second rank tensor), μ_0 and μ_{ij} are permeability of free space and relative permeability, α_{ij} is the linear magnetoelectric coupling. The third rank tensors β_{ijk}, γ_{ijk} represent the higher order (quadratic) magnetoelectric coefficients.

The ME effect can be easily established in the form of $P_i(H_j)$ or $M_i(E_j)$. Thus, $P_i(H_j)$ and $M_i(E_j)$ can be obtained by differentiation of the equation (1.11) with respect to E_i and H_j, respectively.

The induced polarization $P_i(H_j)$ by setting $E_j = 0$ is:

$$P_i(H_j) = -\frac{\partial F}{\partial E_i} = \alpha_{ij} H_j + \frac{\beta_{ijk}}{2} H_j H_k + \ldots\ldots \quad (1.12)$$

Similarly, The induced magnetization $M_i(E_j)$ by setting $H_j = 0$ is:

$$\mu_0 M_i(E_j) = -\frac{\partial F}{\partial H_i} = \alpha_{ji} E_j + \frac{\gamma_{ijk}}{2} E_j E_k + \ldots\ldots\ldots \quad (1.13)$$

The magnetoelectric coupling α_{ij} can be expressed by the relation,

$$\alpha_{ij}^2 \leq \epsilon_0 \mu_0 \in_{ii} \mu_{jj} \quad \ldots\ldots (1.14)$$

The magnetoelectric coupling provides an additional degree of freedom for technological applications and in designing multifunctional actuators, sensors, and memory devices. Other applications include quantum electromagnets and multiple state-logic memory elements while manipulation of the electric polarization (P) by a magnetic field (H) can create magnetically switchable devices in the visible and IR region [30,32–36].

Table 1.1: Comparison between type I and type II multiferroics

Type-I multiferroics	S. N.	Type-II multiferroics
Both ferroelectric polarization (P) and magnetization (M) are primary order parameters which emerge below ferroelectric (T_C) and magnetic (T_N) transition temperatures.	(i)	The ferroelectric polarization (P) is a secondary order parameter and an off-shoot of primary magnetic order parameter (M).
They exhibit large ferroelectric polarization and weak magnetoelectric coupling.	(ii)	These compounds result in weak ferroelectric polarization and strong magnetoelectric coupling.
The magnetic transition temperature of type-I materials is often high and even well above the room temperature.	(iii)	The magnetic transition temperature of type-II materials is well below the room temperature.
Examples: $BiFeO_3$ (T_C ~1103 K, T_N ~ 643 K, P~100$\mu C/cm^2$).	(iv)	Examples: $TbMnO_3$ (T_C ~28K, T_N ~ 41 K, P~10^{-2} $\mu C/cm^2$)

1.14. Spin glasses:

The magnetic systems with frustration, disorder, and randomness lead to spin-glass state [24,41–45]. In spin glasses, the magnetic spins freeze in random direction below a characteristic temperature called spin-glass freezing temperature (T_f). The frustration can be easily understood by considering ferromagnetic and antiferromagnetic nearest-neighbour interactions on a triangular lattice as illustrated in Fig. 1.12 (a). It can be seen from the figure that if all the nearest neighbour interactions are ferromagnetic then it is non-frustrated. However, when the nearest neighbour interactions are antiferromagnetic then frustration come into the picture and this leads to number of degenerate ground states as shown in Fig. 1.12 (b). Historically, the first spin-glass transition was reported in diluted metallic alloy systems with very small concentration of the magnetic ions, for example CuMn, AuFe, AgMn etc [24,41,42]. In such dilute magnetic alloy systems, the magnetic ions are randomly distributed over a non-magnetic metal host matrix shown in

Fig. 1.13 (a). The effective exchange interaction between the localized moments is mediated by the conduction electrons provided by the host metal. The interaction between the localized moments and conduction electrons is commonly known as Ruderman-Kittel-Kasuya-Yosida (RKKY) interaction. This RKKY interaction is a long-ranged, oscillatory in nature, and depends on separation between the magnetic moments (r) i.e. it decaying with inverse of the third power of the r.

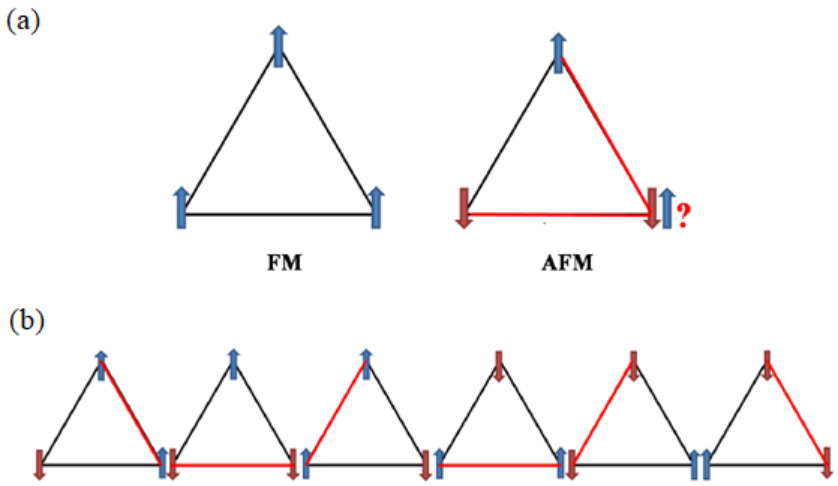

Figure 1.12: Schematic representation of magnetic ground state in a in triangular lattice by considering (a) ferromagnetic and antiferromagnetic nearest neighbour interactions and (b) shows the possible spin arrangement for nearest neighbour antiferromagnetic interactions [45].

The schematic variation of $J_{RKKY}(r)$ interaction with r is depicted in Fig. 1.13 (b). Because of the oscillatory nature, some pairs of spins will experience ferromagnetic interactions and other will experienced antiferromagnetic interaction and therefore, it leads to frustration in the system. Mathematically, the RKKY interaction can be expressed as [42]:

$$J_{RKKY}(r) \propto \cos(2k_F r)/r^3 \qquad \ldots\ldots (1.15)$$

where k_F is the Fermi wave-vector.

In addition to the diluted canonical spin glass systems, spin glass freezing has been observed in concentrated systems also by destroying long-range ordered magnetic

phase through random disorder caused by chemical substitutions [24,41,42]. Further, the compositions close to percolation threshold, the long-range ordered phase have been found to undergo re-entrant type spin-glass transition [42]. Several theories based on random field and random bond models have been proposed to explain the spin-glass transition in such concentrated systems [42].

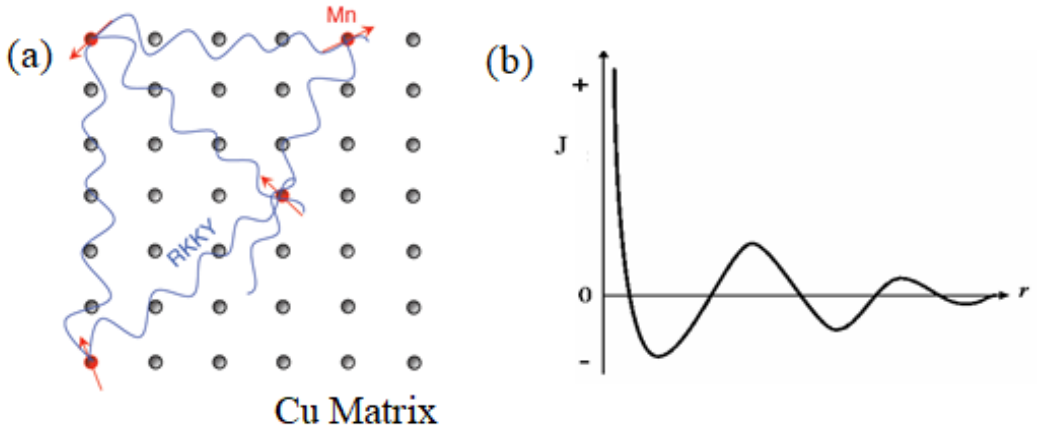

Figure 1.13: (a) Schematic representation of RKKY interactions which take place in dilute metallic spin-glass system like CuMn (b) Schematic variation of $J_{RKKY}(r)$ interaction with separation (r) between the moments.

1.15. Characteristics of spin glasses:

(**a**) The dc magnetization measurement reveals a history dependent irreversibility under zero field cooled (ZFC) and field cooled (FC) conditions below a characteristic temperature called irreversibility temperature (T_{irr}). They also show a sharp peak (cusp) in the ZFC susceptibility at the spin-glass freezing temperature (T_f) while the FC curve shows plateauing below T_f. For canonical spin glass systems like CuMn, AuFe, AgMn, the T_{irr} nearly coincides with T_f [41]. For concentrated systems, the ZFC peak is broader and $T_{irr} > T_f$. Fig. 1.14 depicts the typical dc magnetization curve for a dilute spin-glass system.

(**b**) The second criterion for the spin-glass transition is obtained from the ac susceptibility measurements. Both the dilute and concentrated systems exhibit a sharp anomaly in the ac susceptibility whose peak temperature is found to be frequency dependent i.e., it shifts towards higher temperature side with increasing frequency. This is illustrated in Fig. 1.15 for CuMn system [46]. Usually, for dilute systems the anomaly is quite sharp indicative of a thermodynamic phase transition. The spin dynamics in both dilute and concentrated systems follows critical slowing down with a characteristic spin-glass transition temperature T_{SG} at which the relaxation time diverges and the system become non-ergodic following Vogel-Fulcher or power law type dynamics [24,41–44].

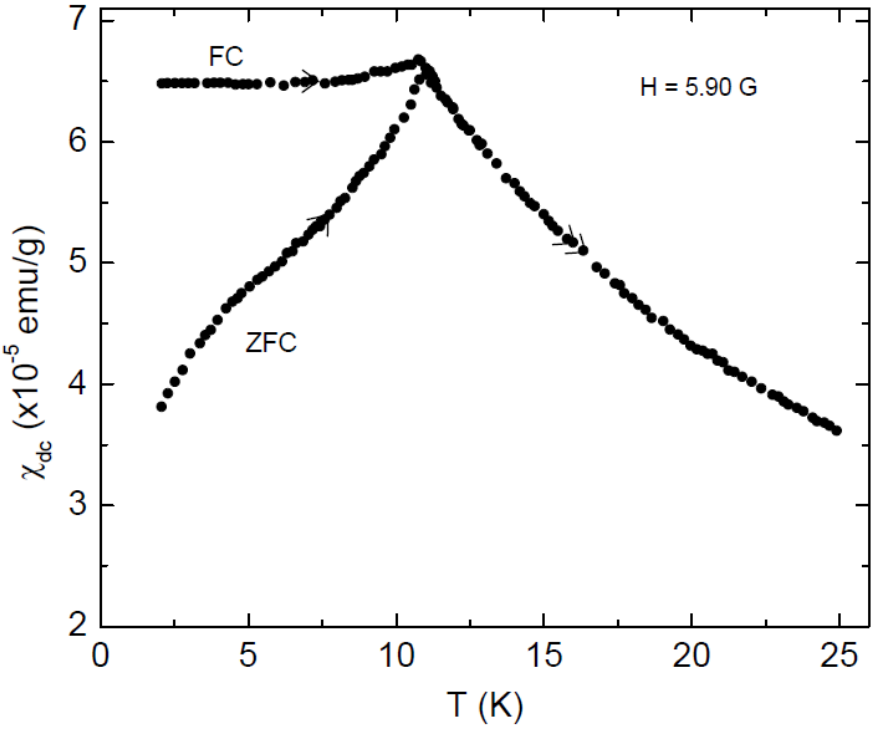

Figure 1.14: Temperature dependence of dc magnetic susceptibility curves of CuMn (3%) system measured under ZFC and FC conditions [46].

(**c**) The third characteristic feature of spin glasses can be obtained from the non-linear susceptibility data. It has been shown that the third harmonic (χ_3) diverges (see Fig. 1.16) at the spin-glass transition temperature (T_{SG}) as per a power law type behaviour [47].

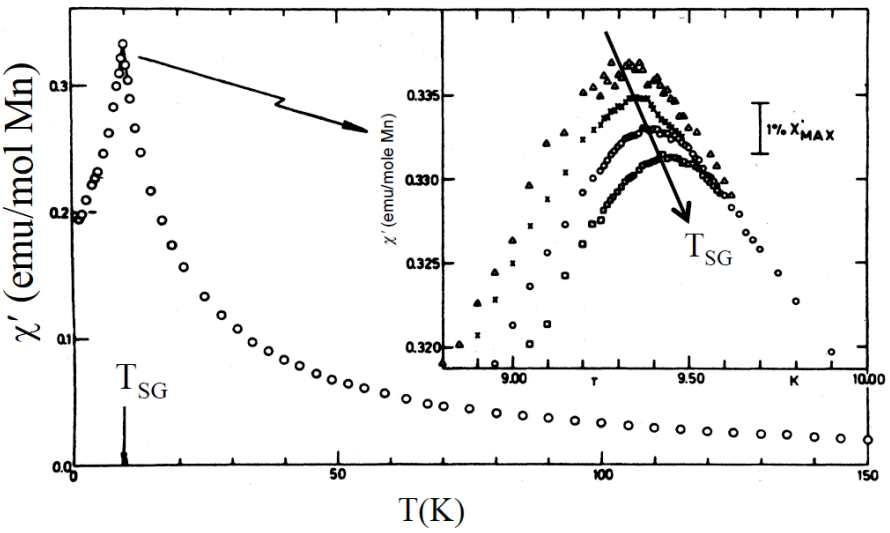

Figure 1.15: Temperature dependence of ac magnetic susceptibility curves of CuMn system showing cusp at T_{SG}. Inset depicts the frequency dispersion across T_{SG} [41].

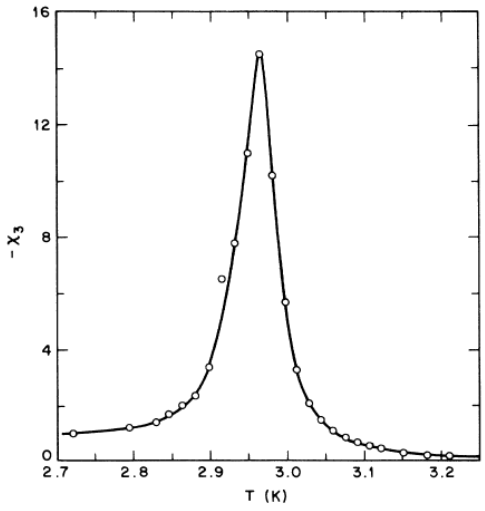

Figure 1.16: Variation of the nonlinear susceptibility (χ_3) as function of temperature across the spin-glass transition at a frequency of 10^{-2} Hz for AgMn system [47].

(**d**) The fourth criteria which are used to characterize the spin-glass state correspond to the presence of slow dynamics, aging, memory and rejuvenation effects in the spin-glass state of both the dilute and concentrated systems. The slow relaxation of magnetization in the spin-glass state follows a stretched exponential behaviour corresponding to a distribution of relaxation times [24,41–44]. The memory and rejuvenation effect in spin-glasses has been captured in dc magnetization measurements as a function of temperature at very low magnetic fields with and without intermediate wait time t_w below the T_{SG}. A hole burning dip is clearly observed at the waiting temperature T_w showing that the dc susceptibility rejuvenates to its original value. This is illustrated in Fig. 1.17 for CuMn system.

(**e**) The fifth characteristics of spin glasses is the field dependent shift of spin-glass freezing temperature T_f along de Almeida-Thouless (A-T) or Gabay-Toulouse (G-T) lines in the T-H plane [49–53]:

$$H^2 = A[1-(T_f(H)/T_f(0))]^m \qquad \text{…….(1.16)}$$

The exponent m is 3 for the A-T line and m=1 for the G-T line.

(**f**) Another criterion which is used for characterizing the spin-glass state is the magnetic contribution to specific heat (C_m). The temperature dependence of C_m shows broad maxima above the spin-glass freezing temperature (T_f) and below this temperature it shows linear behaviour for dilute metallic spin-glass systems shown in Fig. 1.18 [41]. The linear nature of C_m below T_f is explained by using a two-level tunnelling model [24,41,42,44,54]. The broad maxima above T_f can be understood in terms of the release of the magnetic entropy upto about 70-80% above T_f [41] and only 10-20% below T_f.

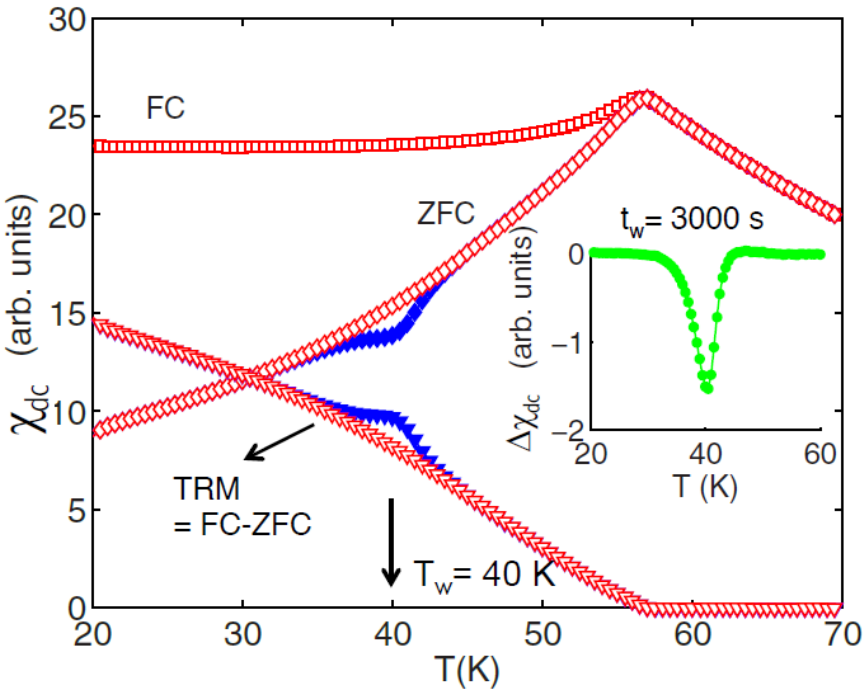

Figure 1.17: Temperature dependence of dc magnetic susceptibility of CuMn system measured at 0.5 Oe field under FC and ZFC conditions. Below T_{SG} =57K, effect of aging, memory and rejuvenation is clearly demonstrated. Inset depicts a "hole burnt" at the waiting temperature (T_w) [48].

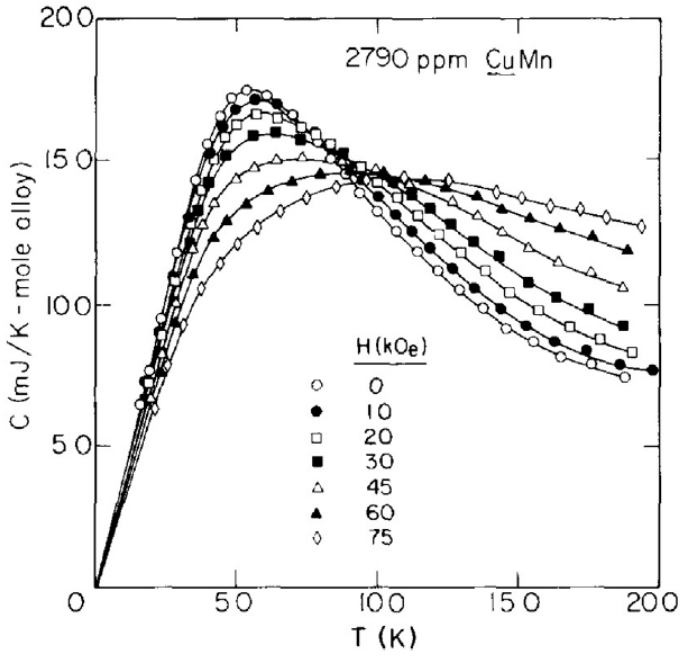

Figure 1.18: Temperature dependence of magnetic contribution to the specific heat (C_m) of CuMn system at various magnetic fields. Here, the T_f is 3.0 K and C_m exhibits maximum at 5K [41].

However, for concentrated spin-glass systems, different models have been proposed at low temperatures: (i) linear temperature dependence of C_m below T_f [55–57], (ii) C_m has been modelled using exponential functions like $C_m = aT^{1/2} \exp(-\Delta E/k_BT)$, $C_m = aT\exp(-\Delta E/k_BT)$, and $C_m = aT^{-2}\exp(-\Delta E/k_BT)$ [58–62], (iii) a power law type dependence of $C_m \sim T^{\alpha}$ with $\alpha = 1.2$ to 2 [63,64].

1.16. Literature Review:

Since in this work, we have investigated the compound bismuth ferrite ($BiFeO_3$), calcium iron niobate ($Ca(Fe_{1/2}Nb_{1/2})O_3$), and solid solution of $BiFeO_3$ with $BaTiO_3$, $Ca(Fe_{1/2}Nb_{1/2})O_3$ with $BiFeO_3$ and $LaFeO_3$, we present a brief review about the structure and properties of these compounds.

1.16.1 $BiFeO_3$ as a type-I multiferroic:

Amongst the multiferroics, $BiFeO_3$, is said to be type-I multiferroic as it not only exhibit ordering of both electric and magnetic dipoles below two different transition (ferroelectric T_C~1103K [65] and antiferromagnetic T_N~643K [66]) temperatures, but also display coupling of the electric and magnetic order. Because of their potential for designing novel multifunctional devices and data storage systems based on the possibility of manipulating magnetization (electric polarisation) by electric (magnetic) field, the interest in multiferroics continues unabetted. $BiFeO_3$ has received considerable attention over the last few decades and the last couple of years have witnessed several new findings on this compound in pure and solid solution forms.

1.16.2 Synthesis and phase diagram of $BiFeO_3$:

The $BiFeO_3$ sample is usually prepared from equimolar mixture of Bi_2O_3 and Fe_2O_3. The phase diagram for Bi_2O_3-Fe_2O_3 is shown in Fig. 1.19 [67,68]. The synthesis of single-phase $BiFeO_3$ sample is very difficult due to the narrow temperature range of the

stability of the perovskite phase and high volatility of Bi leads to formation of secondary phases like $Bi_{36}Fe_2O_{57}$ [69], $Bi_2Fe_4O_9$ [70], $Bi_{25}FeO_{39}$ [71] and $Bi_{46}Fe_2O_{72}$ [72] along with $BiFeO_3$ phase. However, these secondary phases formed during synthesis of $BiFeO_3$ can be leached out by dilute nitric acid [70,71,73]. The formation of such impurity phases has detrimental effect in the physical and magnetic properties of sample, as it increases the conductivity and leakage current of the sample.

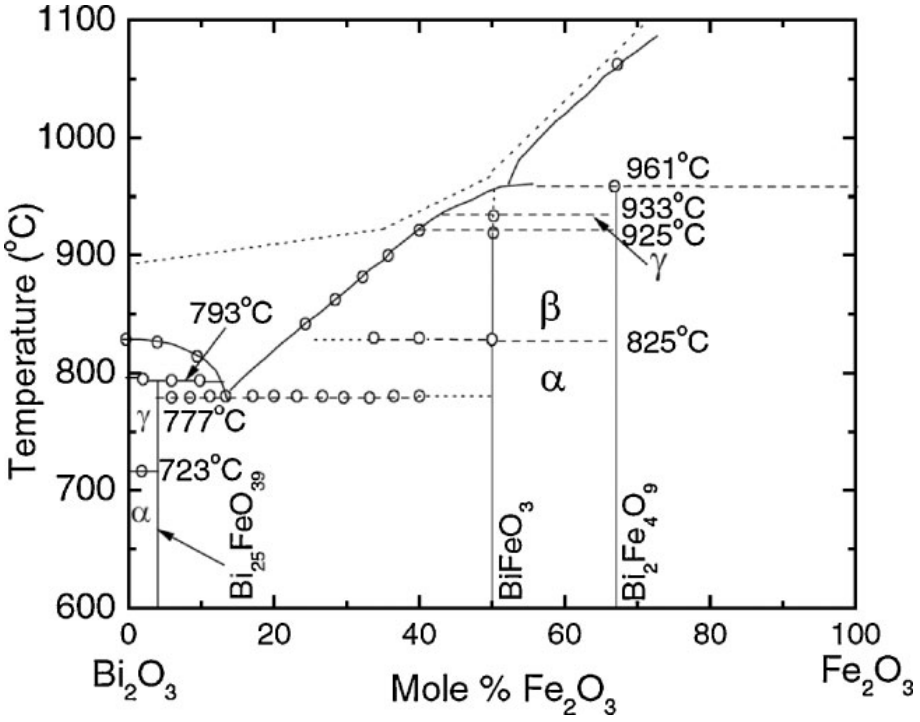

Figure 1.19: Phase diagram of $BiFeO_3$ using ingredients Bi_2O_3 and Fe_2O_3 [67].

1.16.3 Structure and multiferroic properties of $BiFeO_3$:

The room temperature crystal structure of $BiFeO_3$ corresponds to rhombohedrally distorted perovskite structure in the R3c space group [74–76] with $a^-a^-a^-$ tilt system in which the neighbouring oxygen octahedra are rotated anti-clockwise about the $[111]_{pc}$ direction. The cell parameters for R3c structure of $BiFeO_3$ were determined as a=b=5.58102(4), c=13.8757(4), $\alpha=\beta=90$ and $\gamma=120$ [77] in the hexagonal unit cell which contains six formula units (thirty atoms). The primitive unit cell, shown in Fig. 1.20 [78],

contains two formula units (ten atoms), arising from counter-rotations of neighboring oxygen octahedra about the pseudocubic $[111]_{pc}$ symmetry axis. The *R*3*c* symmetry permits the development of a spontaneous polarization along $[111]_{pc}$, and Bi, Fe, and O ions are displaced relative to one another along this threefold axis [77]. The first-principles calculations on the rhombohedral phase of $BiFeO_3$, predicted very high ferroelectric polarization 90–100 $\mu C/cm^2$ [79,80]. Experimentally, very high value of P_s = 60 $\mu C/cm^2$ has been reported along the $[010]_{pc}$ direction (i.e., 100 $\mu C/cm^2$ along the polar [111] direction) of a rhombohedral $BiFeO_3$ single crystal, with high resistivity of $6x10^{10}$ Ohm-cm at room temperature under 100V, grown from a Bi_2O_3-Fe_2O_3 flux method [81], indicating that the high value of polarization is an intrinsic property of the $BiFeO_3$ phase.

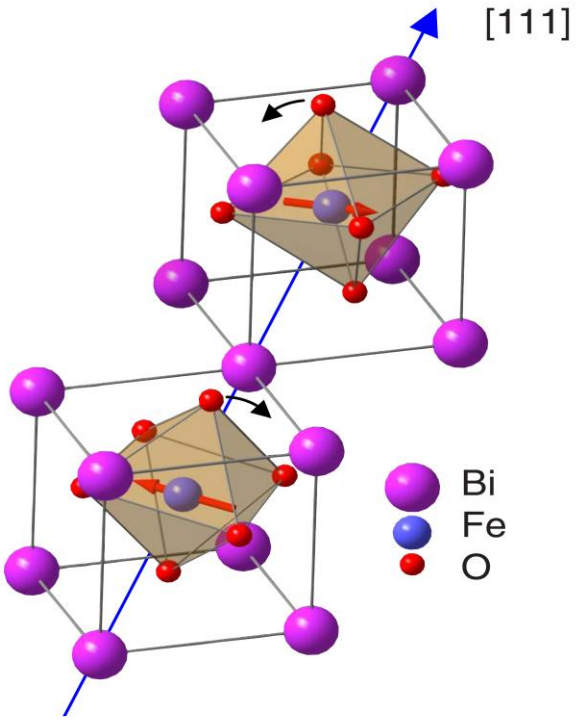

Figure 1.20: Crystal structure of $BiFeO_3$. Two simple perovskite unit cell are shown to illustrate the successive oxygen octahedra along the polar [111] axis rotate with opposite sense. Arrows on Fe atoms indicate the orientation of the magnetic moments in the (111) plane [78].

Apart from ferroelectric behaviour, $BiFeO_3$ is also known to exhibit an antiferromagnetic ordering. The magnetic structure of $BiFeO_3$ first studied by Sosnowska et al. [73] and showed that the Fe magnetic moments are coupled ferromagnetically within the pseudocubic [111] planes and antiferromagnetically between adjacent planes, leading to a G-type antiferromagnetic structure as shown in Fig 1.21 (a). If the magnetic moments are oriented perpendicular to the $[111]_{pc}$ direction (i.e. (111) plane as shown in Fig. 1.20), the symmetry also permits a canting of the antiferromagnetic sublattices resulting in a macroscopic magnetization (according to Dzyaloshinski-Moriya interaction), so-called weak ferromagnetism. However, it was also found that the there is

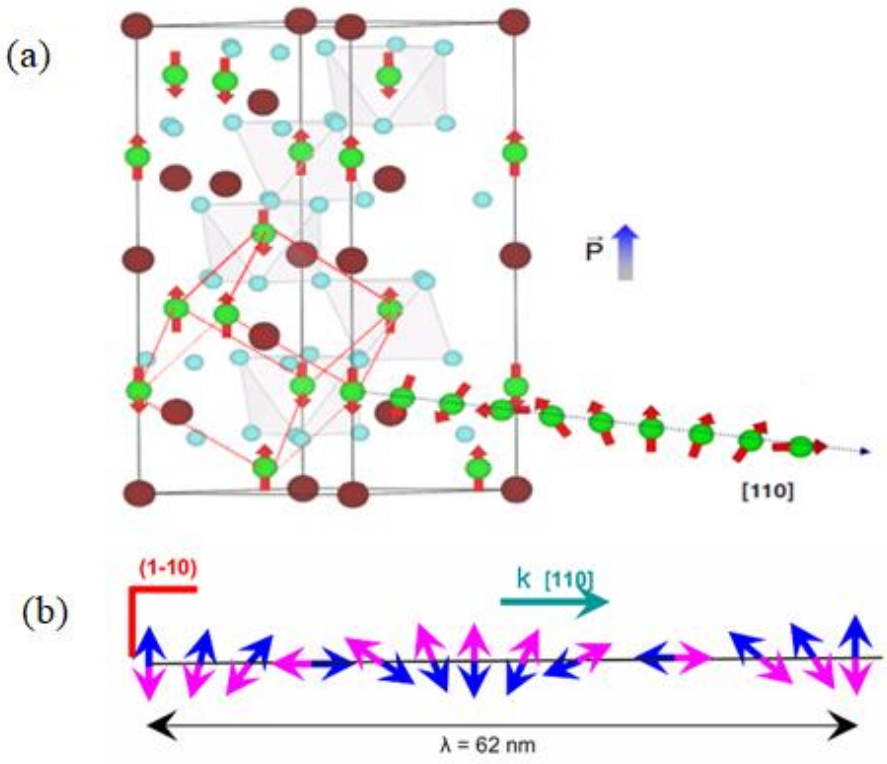

Figure 1.21: (a) Magnetic structure of $BiFeO_3$ [82] (b) The propagation wave vector **k** is along the $[110]_{hex}$ direction and lies in the plane of spin rotation (1-10) [71].

a spin cycloid structure is superimposed on the antiferromagnetic ordering. The spin cycloid propagating along $[110]_{hex}$ direction with an extremely long period of 62 nm and

lies in the plane (1-10) of spin rotation as shown in Fig. 1.21(b) [71,82]. The modulated spiral spin structure leads to cancellation of macroscopic magnetization. Owing to the presence of spiral spin structure, the field and temperature dependent magnetization measurements have been observed to exhibit pure antiferromagnetic response as shown in Fig. 1.22 [71], without any trace of weak ferromagnetism, in $BiFeO_3$ single crystals.

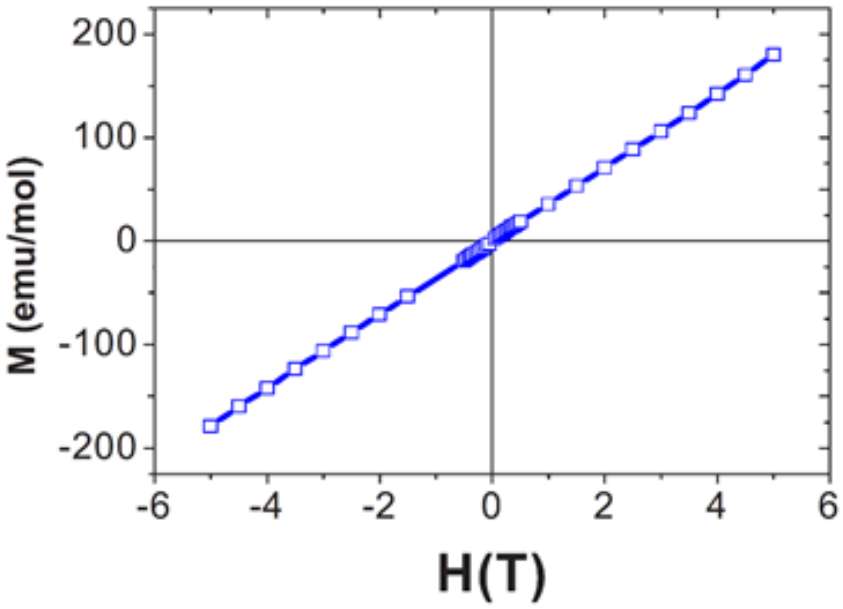

Figure 1.22: M-H hysteresis loop for $BiFeO_3$ measured at room temperature [71].

1.16.4 Magnetoelectric coupling in $BiFeO_3$:

The presence of modulated spin spiral structure in $BiFeO_3$, inhibits the linear magetoelectric coupling and shows only quadratic coupling [83]. However, it has been shown that the modulated spin spiral gets destroyed at a critical field (H_c) of 200 kOe which is illustrated in Fig. 1.23 (a). It is evident from the figure that the measured field dependence of polarization P(H) is quadratic for $H<H_c$ and has a jump at $H=H_c$ when the spiral modulated spin structure is destroyed. Above the critical field H_c, the magnetoelectric polarization changes sign and becomes linearly dependent on magnetic field [84]. The destruction of spin cycloid structure of $BiFeO_3$ by high magnetic field also

results in the release of the latent magnetization with remanent M_r ~0.30 emu/g at 10 K as shown in Fig. 1.23 (b). [84]. The application of high magnetic field greater than 20 T leads to transformation of modulated spin cycloid structure to a homogeneous magnetic structure [84].

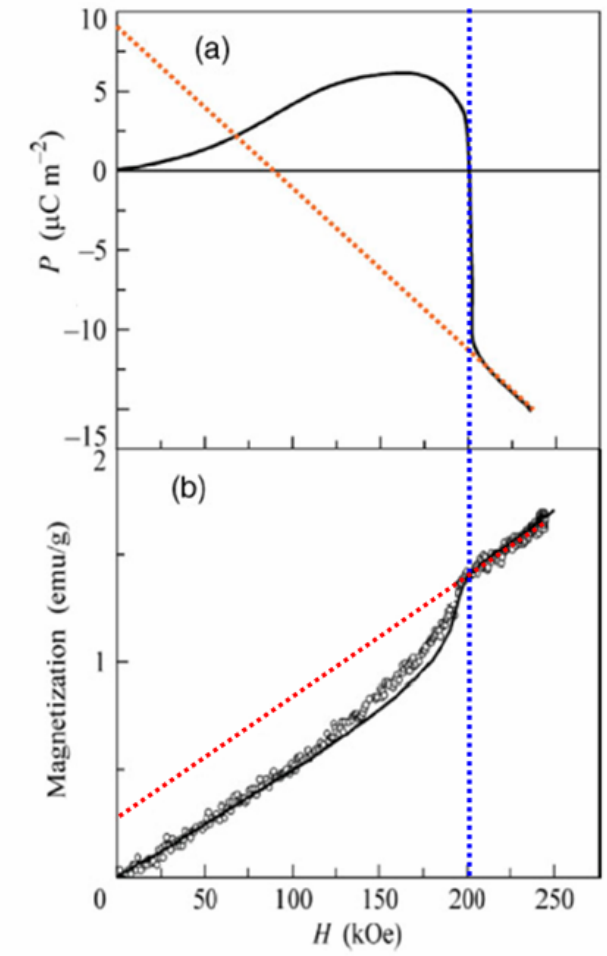

Figure 1.23: (a) Variation of longitudinal polarization with magnetic field at 10 K [84] (b) Magnetization as a function of the magnetic field for H≤25T of a $BiFeO_3$ sample at 10 K [68].

1.16.5 Ferroelectric control of magnetism in $BiFeO_3$:

High resolution neutron diffraction studies on $BiFeO_3$ by two independent groups have shown a relationship between ferroelectric polarization and

antiferromagnetism [85,86]. It is shown that the magnetic moments rotate within the plane defined by (**P**||$[111]_{pc}$) and the spiral propagation vector (**k**||$[10\text{-}1]_{pc}$) as shown in Fig. 1.24 [85]. This has profound consequences: (1) if the direction of polarization is changed by the application of voltage will also rotate the magnetic easy plane. (2) the magnetic easy plane can be switched only if the polarization changes direction, but not if it merely changes polarity, 180^0 switching of the polarization should not affect the magnetic orientation [85].

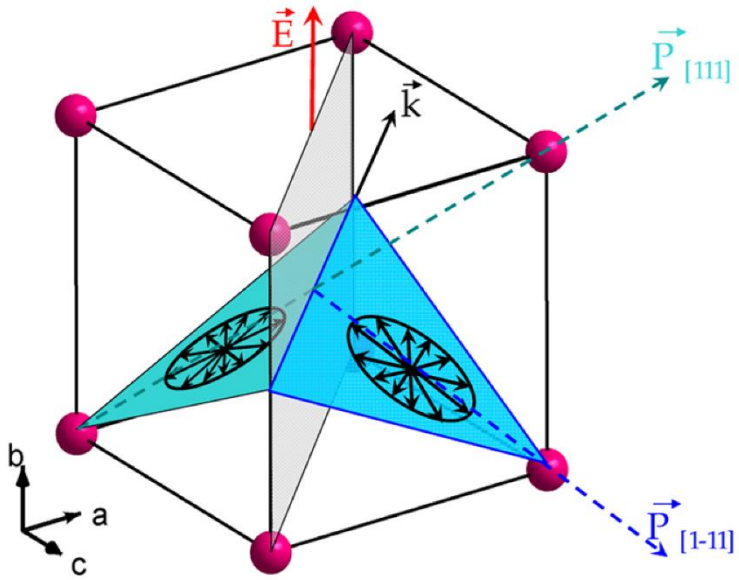

Figure 1.24: Schematic representation of the planes of spiral rotation and spin cycloids **k** vector for the two polarization domains separated by a domain wall [85].

1.16.6 Destruction of modulated spiral spin structure in $BiFeO_3$:

$BiFeO_3$ does not exhibit any macroscopic magnetization due to the presence of spin cycloid structure and thus, inhibit the linear magnetoelectric coupling. In order to observe the macroscopic magnetization and linear magnetoelectric coupling, the spin cycloid need to be destroyed. The spin cycloid of $BiFeO_3$ can be destroyed by: (i) applying high magnetic field in excess of 20T [84], (ii) reducing the particle size below the wavelength (~ 62nm, though the real magnetic structure of the cycloid is

incommensurate) of the spin cycloid [87], (iii) generating strains in epitaxial films due to lattice mismatch [88] and (iv) introducing chemical disorder in the magnetic sublattice [89–93].

The destruction of the spin cycloid due to chemical disorder in the magnetic sublattice of $BiFeO_3$ has been verified in more than one ways: (1) through the absence of the magnetic satellite peaks in the neutron diffraction patterns [90,91,94], (2) observation of weak ferromagnetism through the observation of M-H loops due to the canted G-type antiferromagnetic structure of $BiFeO_3$ [89,90] and (3) observation of linear magnetoelectric coupling [89,90] which is otherwise not permitted in pure $BiFeO_3$ due to symmetry arguments [83].

The constant wavelength and time-of-flight neutron diffraction studies on $BiFe_{1-x}Mn_xO_3$, revealed that the spin cycloid structure of $BiFeO_3$ is modified and changes to homogeneous antiferromagnetic structure beyond x=0.20 concentration (see Fig. 1.25) [76]. Also, in $(Bi_{0.8}Ba_{0.2})(Fe_{0.8},Ti_{0.2})O_3$ system, remnant magnetizations of ~0.15 emu/g, has been reported, as a result of suppression of the spin cycloid [91].

1.16.7 Low temperature magnetic transitions in $BiFeO_3$:

While the nuclear and magnetic structures as well as the multiferroic properties of $BiFeO_3$ at and above the room temperature are well settled [68,95], there exists considerable controversy about various low temperature phenomena that occurs below room temperature. Recent NMR studies suggest that the cycloidal modulation function for the magnetic phase changes from harmonic (sinusoidal) to anhormonic (sn(x, m), elliptic Jacobi function) with m, which is a measure of anhormonicity, increasing from 0.48 at room temperature to 0.95 at 4.2 K [96–99].

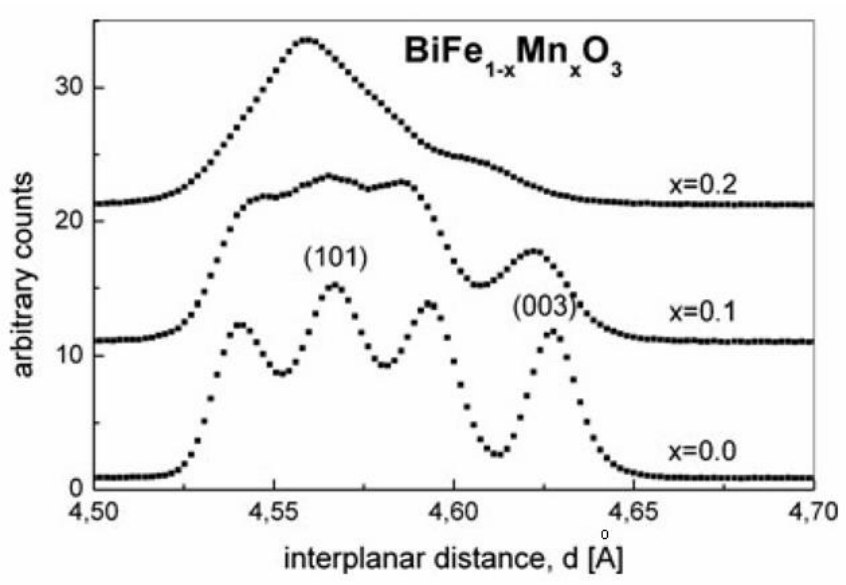

Figure 1.25: Composition dependence of magnetic satellite reflections measured using OSIRIS diffractometer at ISIS for $BiMn_xFe_{1-x}O_3$ [76].

The neutron diffraction studies, which probe the space and time averaged magnetic structure at the bulk level, have also confirmed anhormonic nature of modulation of the cycloid at low temperatures [100,101] but the anhormonicity is found to be much less, 0.50 [100] and <0.25 [101] in two independent studies using single crystals and polycrystalline samples, respectively, than that reported using a local probe like NMR. However, it is hard to imagine that the spin cycloid involving all the spins in the magnetic structure of $BiFeO_3$ will remain unaffected despite the several low temperature phase transitions that have been reported. Using a variety of measurement probes like DC magnetic susceptibility (χ_{DC}) [87,102–107], AC magnetic susceptibility ($\chi'_{AC}(\omega,T)$ and $\chi''_{AC}(\omega,T)$) [102,108], differential scanning calorimetry (DSC) [103] differential thermal analysis (DTA) [109], Raman scattering [110–116] dielectric studies [109,117] and elastic modulus spectroscopy [109,115], several low temperature magnetic transitions have been reported in the temperature range 20 to 25K [102,108], 50-60K [87], 140-150K [103,111,112,116] and 220 to 250 [103] (see Fig. 1.26). Taking into account the observations made by different experimental probes discussed above, the

transitions occurring around 50-60 K, 140–150 K and 220–250 K have been attributed to magnetic but glassy with magnetoelectric coupling, predominantly magnetic transition involving spin reorientation, and antiferromagnetic (AFM) to spin glass (SG) transition with weak coupling with polarization, respectively [103,109]. Another transition reported around 178 – 200 K has been proposed to be magnetoelastic in nature with a small coupling to polarization [109]. Finally, the transition at 20-25K has been reported to be due to a spin glass freezing [102,108]. Towards understanding the true ground state of $BiFeO_3$, it is therefore important to settle if the low temperature phase transitions reported below room temperature are intrinsic to $BiFeO_3$ or some of them could be induced due to the presence of ionic vacancies created during high temperature processing. The present work was undertaken to address this issue.

The spin-glass freezing around 25K in $BiFeO_3$ has several intriguing features in AC χ (ω, T). Firstly, the peak height of $\chi'(\omega, T)$ increases with increasing frequencies which is unusual as the susceptibility always decreases with increasing frequency except near frequencies corresponding to a resonant absorption that may be linked with the resistance, capacitance and inductance of the entire circuit rather than just the sample. Further, the imaginary part $\chi''(\omega, T)$ shows negative cusps at T_f with a peak temperature above the corresponding peak temperature for the real part $\chi'(\omega, T)$. The negative value clearly suggests that the circuit is no longer purely inductive except at very low temperatures (< ~10K). The third intriguing aspect of the $\chi''(\omega, T)$ is the presence of a tiny peak around 10K below which the imaginary part shows positive value. All these features have been tentatively attributed to the LRO AFM phase with modulated magnetic structure that coexists with the SG phase [108], as they are not observed in the conventional spin-glass systems. Further, the occurrence of a spin-glass phase in a

homogeneously ordered system like $BiFeO_3$ without any quenched impurity and randomness is equally intriguing.

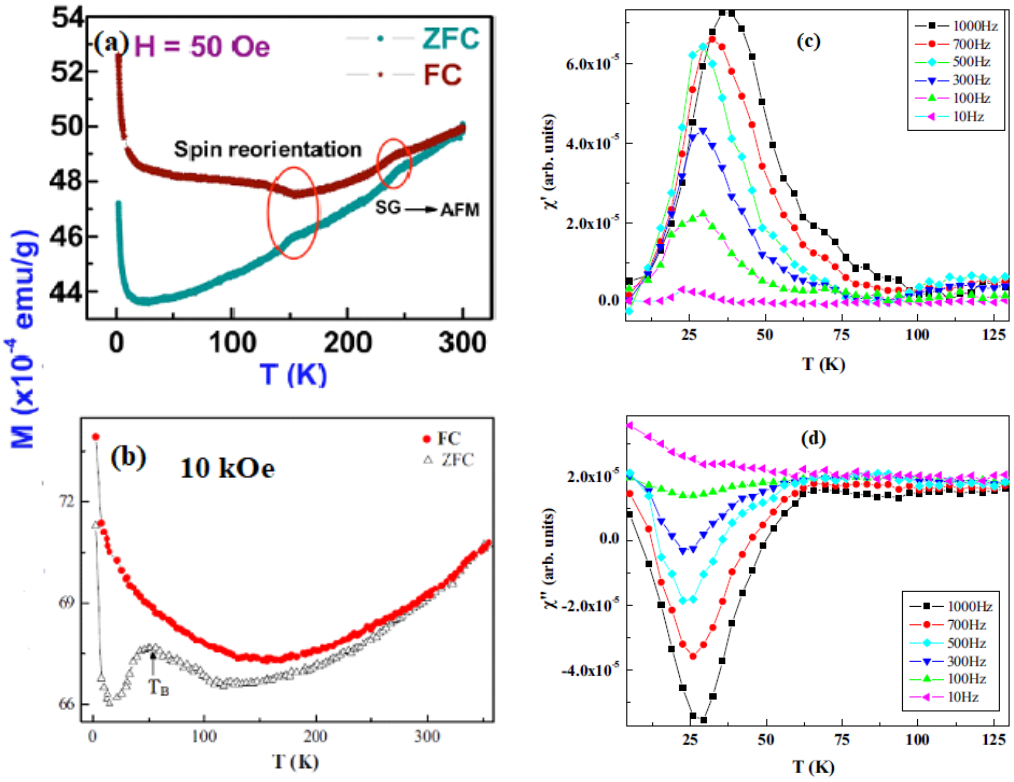

Figure 1.26: Left panel (a) and (b) show the temperature dependence of dc magnetization curves for polycrystalline and single crystals of $BiFeO_3$ measured under ZFC and FC conditions. Right panel (c) and (d) depicts the real and imaginary parts of ac susceptibility of single crystals of $BiFeO_3$ [102,103].

The existing models of spin-glass transitions are based on the concept of disorder, randomness and frustration [24,42–45] although in recent years several ordered systems like manganites h-$DyMnO_3$ [118], hydronium jarosites $(H_3O)Fe_3(SO_4)_2(OH)_6$ [119], herbertsmithite $Co_3Mg(OH)_6Cl_2$ [120], edwardsite $Cd_2Cu_3(OH)_6(SO_4)_24H_2O$ [121], and pyrochlores ($Tb_2Mo_2O_7$, $Y_2Mo_2O_7$, and $Mn_2Sb_2O_7$) [122–124] have been shown to exhibit SG transition. However, these ordered systems are different from $BiFeO_3$ as they all show frustrated interactions due to geometrical reasons. Thus more work is required to

understand the true ground state of $BiFeO_3$. We have addressed some of these issues in chapters II, III and IV.

1.16.8 $BiFeO_3$ solid solutions:

Despite the advantage of room temperature multiferroic properties of $BiFeO_3$, the use of this material for potential applications is limited due to following reasons (i) difficult to synthesize in pure phase form, (ii) low insulating resistance and (iii) weak quadratic magnetoelectric coupling as the presence of the spin cycloid does not allow linear magnetoelectric coupling to develop [84].

In recent years, attempts have been made to synthesize single phase $BiFeO_3$ based solid solutions with a view to destroy the modulated spin cycloid structure and enhance the ferroelectric and magnetic properties. The formation of solid solutions of $BiFeO_3$ with other perovskite oxides such as $BaTiO_3$ [89–91,125],$Pb(Fe_{1/2}Nb_{1/2})O_3$ [94], $PbZrO_3$ [126], $Pb(Zr_xTi_{1-x})O_3$ [127,128], $SrTiO_3$ [129], $CaTiO_3$ [130], $PbTiO_3$ [131], $BiCoO_3$ [132], $NaNbO_3$ [133] and $BiMnO_3$ [134] has been explored. Apart from the enhanced multiferroic properties when forming the solid solutions, $BiFeO_3$ solid solutions exhibit different crystallographic phases and interesting phase transitions with increasing concentration of the disorder [135]. Most importantly, the spin cycloid of $BiFeO_3$ is destroyed in most of these solid solutions leading to the release of the latent weak ferromagnetic magnetization due to spin canting locked in the spin cycloid [89,90,94]. As a result, these solid solutions exhibit linear magnetoelectric coupling.

1.16.9 $BiFeO_3$-$BaTiO_3$ solid solution:

Amongst the $BiFeO_3$ based solid solution systems, the (1-x)$BiFeO_3$-x$BaTiO_3$ or BF-xBT solid solutions have received considerable attention due to large ferroelectric polarization [89,90,136–142], large remnant magnetization [91–93,143], linear

magnetoelectric coupling [89,90] and the highest depolarization temperature for piezoelectric applications [136,139,140,144]. This system also exhibits a variety of phase transitions such as morphotropic phase transition, relaxor ferroelectric phase transition, non-relaxor type diffuse phase transition, tricritical transition, isostructural phase transition and trigger type transitions [91,135,145,146]. More recently Singh et al. presented the ferroelectric and magnetic phase diagram of $BiFeO_3$-$BaTiO_3$ system as a function of temperature and composition above room temperature [146]. It is evident from Fig. 1.27 that increasing the $BaTiO_3$ content (x) in $BiFeO_3$ leads to a structural change from the *R*3*c* phase of pure $BiFeO_3$ to an average cubic structure with the *Pm*-3*m* space group at a critical composition $x \approx 0.35$. With further increase in $BaTiO_3$ content, there is another critical composition around $x \approx 0.85$ at which this cubic phase changes to the tetragonal phase of $BaTiO_3$. The pseudocubic phase is stable in the composition range $0.35 \leq x \leq 0.85$ and show local monoclinic distortion [91,135,145]. Using MnO_2 doping [89,90,136–142], in the BF-xBT system, impressive piezoelectric coefficients have been reported. Further, the piezoelectric property persists up to T_d ~750K without any depoling characteristics in contrast to the commercial toxic Pb^{2+} based $Pb(Zr_xTi_{1-x})O_3$ ceramics which dipole below T_d ~ 400K only. Thus BF-xBT system has emerged as an important Pb-free high temperature piezoelectric material.

1.16.10 Complex perovskites and their multiferroic behaviour:

Among the disordered perovskite systems, there is a big family of $A(B'B'')O_3$ type compounds where the B-site cations may be ordered or disordered depending upon their size and charge differences but the ratio of B':B'' is fixed like 1:1, 1:2, 1:3, as in compounds [147–151]. Such site and charge disordered and ordered compounds with one of the B' site cation being a 3d transition metal element (Sc, Ti, V, Cr, Mn, Fe, Co, Ni etc) with B' and B'' in 1:1 ratio have received immense attention from the point of view of

their properties like colossal magnetoresistance (CMR) [152–154], half metallicity [155–157], metal insulator transition [158–160], superconductivity [161,162], normal ferroelectricity [150] and relaxor ferroelectricity [18,19,163–165], long-range magnetic

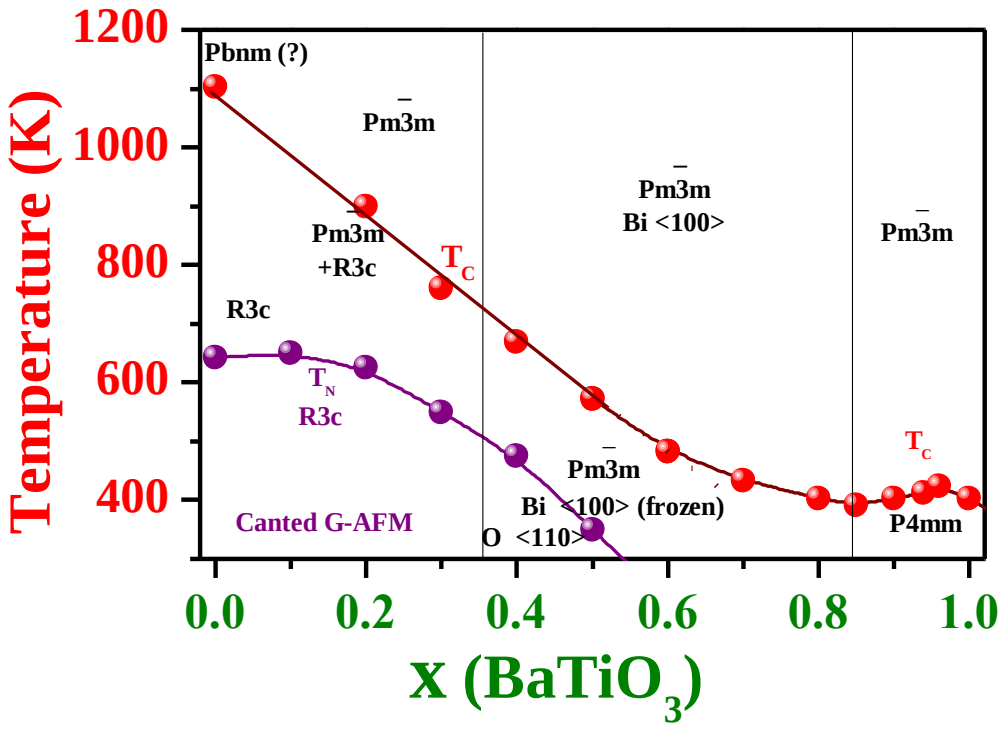

Figure 1.27: Phase diagram of (1-x)$BiFeO_3$-x$BaTiO_3$ system [146].

ordering [166–172] and spin glass (SG) transition [169,171–178], and multiferroicity [179–182]. Historically, the complex perovskites compounds with general formula A(B'B")O_3 where A = Pb, Ba, Sr, Ca and B' and B" are magnetic (Cr, Mn, Fe, Ni, Co, etc.) and non-magnetic (Nb, Ta, W, Sb etc.) transition metal elements, were first synthesized by Russian scientists nearly six decades back with the aim that these compounds can show multiferroicity [183,184]. From this approach, the lead iron niobate $Pb(Fe_{1/2}Nb_{1/2})O_3$ (PFN) emerged as a model type-I multiferroic compound [171,172,185–190].

1.16.11 Lead (Pb)-based complex perovskites:

The Pb-containing compounds like $Pb(Fe_{1/2}Nb_{1/2})O_3$ (PFN), $Pb(Fe_{1/2}Ta_{1/2})O_3$ (PFT), and $Pb(Fe_{2/3}Nb_{1/3})O_3$ (PFW) are known to exhibit relaxor ferroelectric or diffuse ferroelectric transition above room temperature [188,189], G-type antiferromagnetic order below T_N~150K [190] and a spin-glass phase below ~10K [171,172], respectively. The room temperature crystal structure along with the ferroelectric (T_c), magnetic (T_N) and spin-glass transition (T_{SG}) for these compounds are compared in Table 1.2 [171,172,174,176–178,191,192]. There is a recent report on $Pb(Fe_{1/2}Sb_{1/2})O_3$ (PFS) which reveals relaxor ferroelectric behaviour in this compound with T_c~250K and spin-glass transition around ~150K [193]. Fig. 1.28 depicts the temperature dependence of dc magnetic susceptibility measured at 100 Oe field in worming cycle under ZFC and FC conditions for PFN. The ZFC and FC curve clearly reflect the AFM phase transition T_N~144K and below 10K [171,172], the two curves diverges, which is a characteristic feature of spin glasses. Further, the AFM phase transition in PFN is manifested by jump in the temperature dependent dielectric constant [194] and anomalies in the lattice parameters [189]. Interestingly, the LRO AFM phase is found to coexist with the SG phase below T_f ~10K but there is a controversy about the exact origin of the coexistence of the two phases [171,172]. Two different models have been proposed in the literature [171,172]. According to the first model, which is based on macroscopic measurements, the LRO AFM phase results from the infinite percolative clusters of Fe^{3+} spins while the glassy phase is a consequence of the freezing of the finite size isolated clusters with uncompensated Fe^{3+} spin [171] (see Fig. 1.29(a)). This model implies that the SG and LRO AFM phases occur on two separate sublattices. In the second model based on neutron scattering and Mossbauer probes, the SG phase result from the LRO AFM sub-lattice system itself due to freezing of the transverse component of the spin in a

glassy manner [172]. We shall return to this controversy in more detailed in chapter V. The measured temperature dependence of the integrated intensity of the AFM peak at Q =(½, ½, ½) of PFN is shown in Fig. 1.29 (b). It can be seen from this figure that the below the AFM transition, the intensity of the magnetic Bragg peak increases very smoothly but a small decrease in the integrated intensity of AFM peak is observed below 50K, which has been attributed to spin-canting and transverse spin freezing [172].

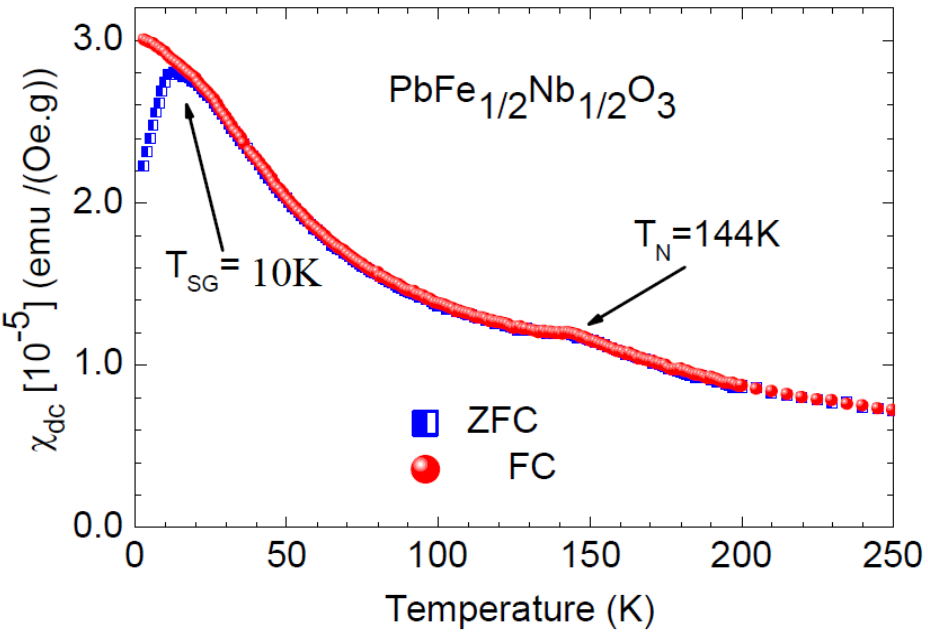

Figure 1.28: Temperature dependence of dc magnetic susceptibility curves of $Pb(Fe_{1/2}Nb_{1/2})O_3$ measured under ZFC and FC conditions [172].

1.16.12 Pb-free complex perovskites:

The Pb-free complex perovskites with a general formula of $A(Fe_{1/2}B'_{1/2})O_3$ type with A = Ba, Sr, Ca and B' = Nb, Ta, and Sb do not display LRO ferroelectric and AFM phases, despite Nb^{5+} being a ferroactive ion of $4d^0$ type [37] and the concentration of $3dFe^{3+}$ moments at the B-site being higher than the critical percolation threshold value [195–197]. However, these Pb-free complex perovskite niobates and tantalates are reported to exhibit SG freezing at low temperatures with T_f ~25K [176–178] similar to

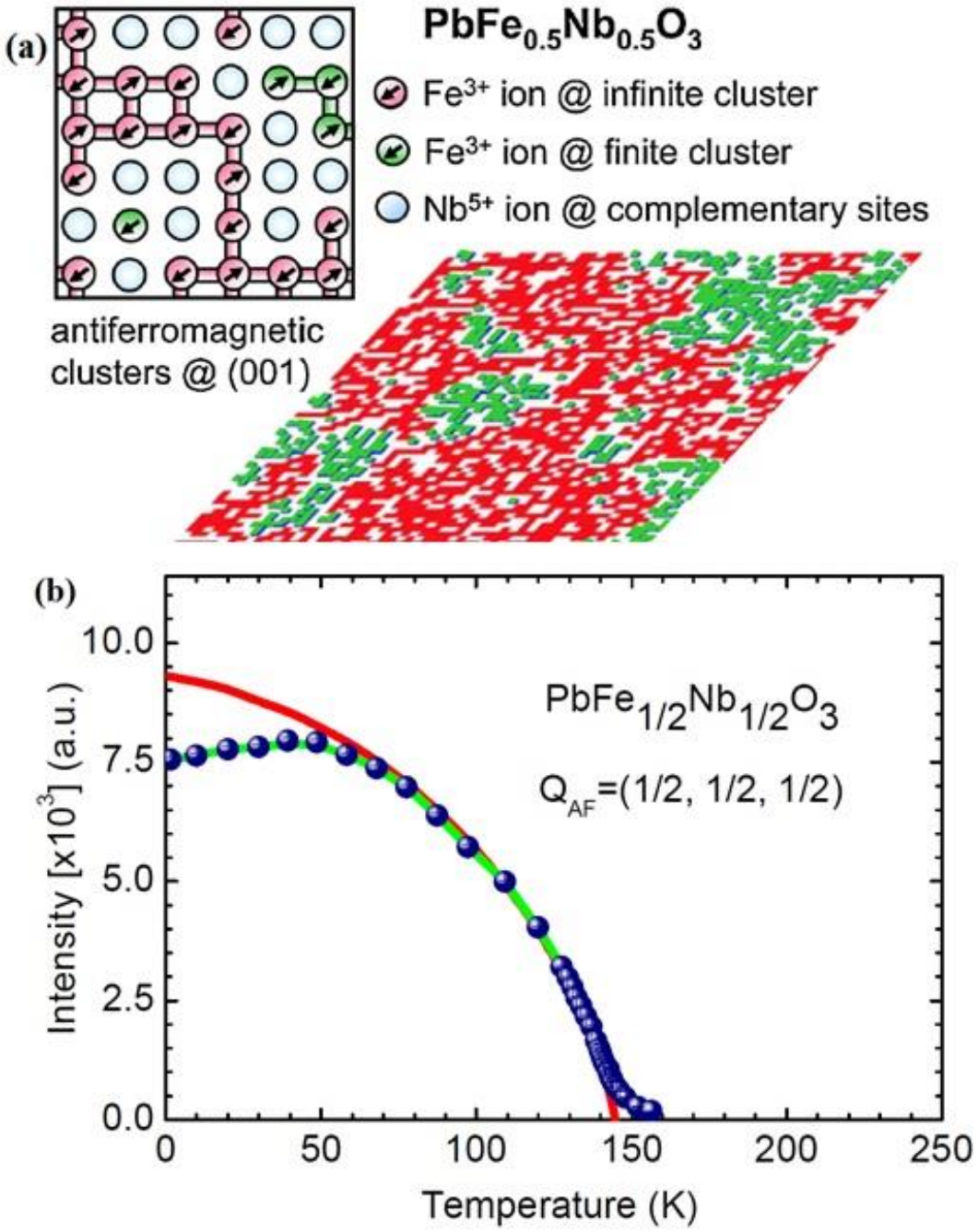

Figure 1.29: **(a)** Schematic representation of the antiferromagnetic Fe^{3+} clusters in $Pb(Fe_{1/2}Nb_{1/2})O_3$ with projections of <111>-oriented spins viewed in (001) cross sections at different scales [171] and **(b)** Temperature dependence of the integrated intensity of the antiferromagnetic (AFM) peak intensity of PFN at Q = (½, ½, ½) [172].

PFN though with a slightly higher T_f which is ~10K for PFN and PFT. Unlike the Nb and Ta based compounds, the spin glass freezing temperature T_f of Sb based complex perovskites, $Ca(Fe_{1/2}Sb_{1/2})O_3$ (CFS), $Sr(Fe_{1/2}Sb_{1/2})O_3$ (SFS), $Ba(Fe_{1/2}Sb_{1/2})O_3$ (BFS), is a little lower 17K, 20K, 16K [176,178], respectively, as compared to their niobates and tantalate counterparts.

This difference has been attributed to the partial 1:1 chemical ordering of the $Fe^{3+}$and Sb^{5+} ions at the B-site [178]. The so-called spin-glass transition in the lead-free complex perovskites has not been thoroughly investigated, except for the observation of bifurcation of the ZFC and FC dc magnetization M(T) plots with a peak in the ZFC data, and therefore the true nature of this transition may be different. Fig. 1.30 shows temperature dependence of dc susceptibility of $Ca(Fe_{1/2}Nb_{1/2})O_3$ measured at 1000 Oe field under ZFC and FC protocols [176]. It is evident from the figure that the ZFC and FC curves bifurcate below T_f~25K suggesting the spin-glass behaviour [24,41] but such a bifurcation can also occur due to superparamagnetic blocking [198]. We have carried out a comprehensive study of the spin-glass transition in $Ca(Fe_{1/2}Nb_{1/2})O_3$ using macroscopic and microscopic probes and the results are discussed in detail in chapter V. The room temperature crystal structure along with the spin-glass freezing temperature of Pb-free compounds are compared in Table 1.2 [176–178]. It is interesting to note that the Pb^{2+} and Ba^{2+} based $A(Fe_{1/2}B_{1/2})O_3$ compounds exhibit normal perovskite structure where as Ca^{2+} and Sr^{2+} based compounds exhibit tilted oxygen octahedra. As a result, the unit cell of the later is doubled giving rise to characteristic superlattice peaks [176,199,200]. Superlattice peaks in such compounds has also been reported due to cations ordering of the Fe^{3+} and Sb^{5+} at the B-site for some compounds [201,202]. It is worth mentioning that the room temperature crystal structure of $Ca(Fe_{1/2}Nb_{1/2})O_3$ is controversial as two different space group symmetries (Pbnm (orthorhombic) and $P2_1/n$ (monoclinic)) have

been reported using laboratory XRD data [176,199–202]. We have addressed this controversy using synchrotron x-ray diffraction data in chapter V. The presence of LRO AFM phase in PFN has been attributed to the presence of Pb^{2+} with $6s^2$ lone pair electrons which may mediate the next nearest neighbour superexchange pathways in pure PFN along the <111> pc directions [203]. However, this hypothesis needs to be tested by more careful analysis of the Pb-free niobate compounds like CFN around the expected AFM T_N~150K. This is subject matter of chapter VI.

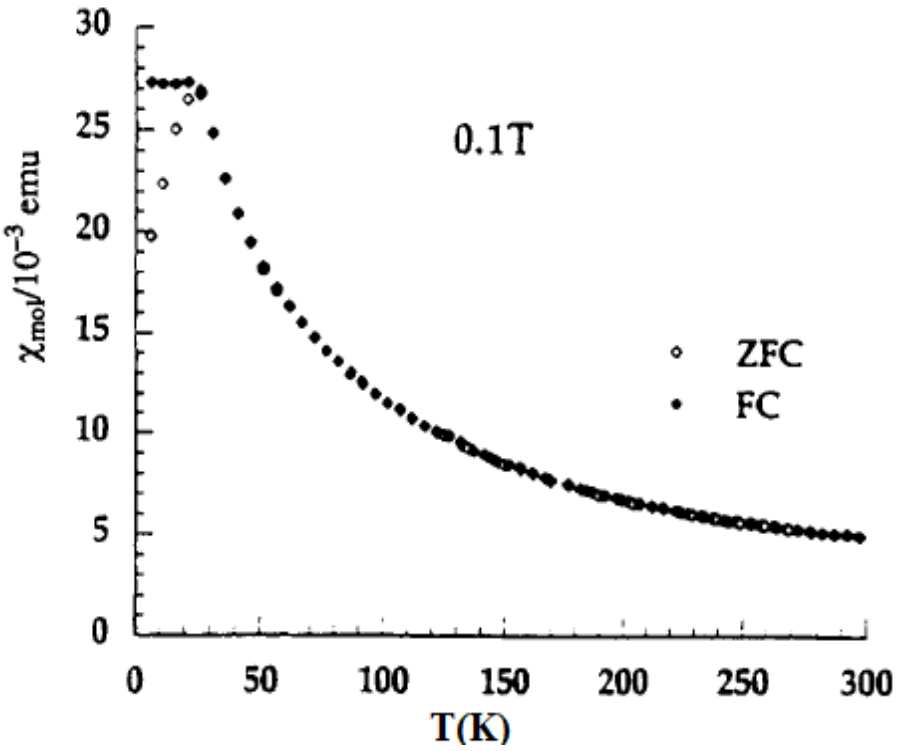

Figure 1.30: Temperature dependence of dc magnetic susceptibility curves of $Ca(Fe_{1/2}Nb_{1/2})O_3$ measured under ZFC and FC conditions [176].

Table 1.2: Comparison of room temperature crystal structure, spin-glass freezing (T_f) temperature, ferroelectric transition temperature (T_c), antiferromagnetic transition temperature (T_N) of complex perovskites.

Complex Perovskite	**Crystal Structure**	**Chemical Ordering at B-site**	**T_f /T_{SG} (K)**	**T_N (K)**	**T_c (K)**	**Reference**
$Pb(Fe_{1/2}Nb_{1/2})O_3$	Monoclinic (Cm)	Disordered	10	150	385	[171,172]
$Pb(Fe_{1/2}Ta_{1/2})O_3$	Cubic (Pm-3m)	Disordered	10	150-180	240	[174]
$Pb(Fe_{2/3}W_{1/2})O_3$	Cubic (Pm-3m)	Disordered	10	350	150	[191]
$Pb(Fe_{1/2}Sb_{1/2})O_3$	Cubic (Fm-3m)	Ordered	25	-	-	[192]
$Ca(Fe_{1/2}Nb_{1/2})O_3$ (Previous work)	Orthorhombic (Pbnm) and Monoclinic ($P2_1/n$)	Disordered/Ordered	24±1	-	-	[176,199–202]
$Ca(Fe_{1/2}Nb_{1/2})O_3$	**Orthorhombic (Pbnm)**	**Disordered**	**25**	**-**	**-**	**(Our Work)**
$Ca(Fe_{1/2}Ta_{1/2})O_3$	Orthorhombic (Pbnm)	Disordered	23±1	-	-	[176]
$Ca(Fe_{1/2}Sb_{1/2})O_3$	Orthorhombic (Pbnm)	Disordered	17±1	-	-	[176]
$Sr(Fe_{1/2}Nb_{1/2})O_3$	Tetragonal (P4/mcm)	Disordered	25±1	-	-	[176–178]
$Sr(Fe_{1/2}Ta_{1/2})O_3$	Orthorhombic (Pbnm)	Disordered	23±1	-	-	[176]
$Sr(Fe_{1/2}Sb_{1/2})O_3$	Monoclinic ($P2_1/n$)	Ordered	20	-	-	[178]
$Ba(Fe_{1/2}Nb_{1/2})O_3$	Cubic (Pm-3m)	Disordered	25±1	-	-	[176–178]
$Ba(Fe_{1/2}Ta_{1/2})O_3$	Cubic (Pm-3m)	Disordered	22±1	-	-	[176–178]
$Ba(Fe_{1/2}Sb_{1/2})O_3$	Hexagonal ($P6_3/mmc$)	Ordered	16	-	-	[178]

1.17. Objective of the present thesis:

This thesis is an attempt to understand the nature of low temperature magnetic transitions in $BiFeO_3$ (BF) and $Ca(Fe_{1/2}Nb_{1/2})O_3$ (CFN) on one hand and some of their solid solutions $(1-x)BiFeO_3$-$xBaTiO_3$ (BF-xBT), $(1-x)Ca(Fe_{1/2}Nb_{1/2})O_3$-$xBiFeO_3$ (CFN-0.10BF) and $(1-x)Ca(Fe_{1/2}Nb_{1/2})O_3$-$xLaFeO_3$ (CFN-0.10LF), on the other.

As discussed in section 1.11.7, there are several controversies about the spin-glass transition reported in $BiFeO_3$ as some workers believe that it is due to the presence of impurity phase spin clusters. Further, no attempt has been made to understand the effect of disorder on the spin-glass transitions reported in $BiFeO_3$. We have addressed these issues in chapters II, III and IV using both macroscopic (M(T), χ (ω, T), M(H), M(t), ε'(T) etc) and microscopic (neutron and x-ray diffraction) probes. We show that these spin glass transitions are intrinsic to the system based on the observation of magnetoelastic and magnetoelectric couplings at the spin-glass transitions. Our work has led to the discovery of a succession of two spin-glass transitions in BF-xBT system resulting from the freezing of the transverse and longitudinal components of the spins. We have also shown that both the spin-glass phases coexist with the LRO AFM phase in perfect agreement with the theoretical predictions for disordered Heisenberg systems. Further, we have discovered magnetoelectric and magnetoelastic character of the two spin-glass phases for the first time. We have also presented first ever evidence for phase coexistence using specific heat measurements.

The second major objective of the present thesis was to confirm the existence of spin-glass phase in Pb-free complex perovskites taking $Ca(Fe_{1/2}Nb_{1/2})O_3$ as an example using multiple criterion that are used in the literature. The spin-glass state in this system was also investigated from the point of view of the controversies related to the origin of spin-glass phase in the related compound $Pb(Fe_{1/2}Nb_{1/2})O_3$, as discussed in section

1.15.11 Chapter V of this thesis is dedicated to this aspect. We show in this chapter that $Ca(Fe_{1/2}Nb_{1/2})O_3$ undergoes cluster spin-glass freezing involving short-range ordered (SRO) AFM spin clusters.

The third major objective of this work was to go deeper into the behaviour of Pb-free complex perovskite like $Ca(Fe_{1/2}Nb_{1/2})O_3$ to get an insight into the real reason for the absence of LRO AFM state in contrast to their Pb-based counterparts like $Pb(Fe_{1/2}Nb_{1/2})O_3$. Using DC magnetization and neutron scattering studies, we show that $Ca(Fe_{1/2}Nb_{1/2})O_3$ is an incipient AFM with a potential for undergoing AFM transition around $T_N \sim 175K$. We present evidence for the stabilization of this AFM phase through 10% $BiFeO_3$ or $LaFeO_3$ substitution which enables $Ca(Fe_{1/2}Nb_{1/2})O_3$ to acquire the critical percolation threshold concentration of Fe^{3+} spins in the magnetic sublattice.